CDDpress

www.nature.com/cdd

ARTICLE OPEN

Mutant Huntingtin disrupts neurogenic and astroglial programs via the EZH2–Let-7g–LIN28 axis with rescue by epigenetic modulators

JD Rosati[1,2]✉, A. Casamassa[1,28], G. Ruotolo[1,28], AMG Giovenale[1,28], D. D'Andrea[3], G. Rotundo[1], A. D'Anzi[1], EM Turco[1], G. Bergonzoni[4], A. Visioli[5], I. Lombardi[6], RM Carletti[7], U. Cappucci[8], AM Casale[8], A. Migazzi[9], M. Ciavarella[10], A. Rinaldi[11], C. Bertollini[12], V. Giambra[13], A. De Luca[14], D. Rotili[15,16], S. Valente[17], E. Binda[18], O. Palumbo[19], M. Gelati[20], F. Squitieri[21], L. Piacentini[8], D. Ferrari[6], S. Di Angelantonio[11,22], M. Catalano[11], A. Mai[17], M. Biagioli[4], M. Basso[9], M. Pennuto[23,24], B. Reynolds[25] and AL Vescovi[26,27]✉

© The Author(s) 2026

The molecular mechanisms by which mutant huntingtin (mHTT) drives pathogenesis in Huntington's disease (HD) remain incompletely defined. Here we show that neurogenesis is disrupted at multiple stages of lineage progression in both rodent and human neural stem cell (NSC) models of HD. We identify a previously unrecognized phenotype characterized by aberrant expansion of early multipotent progenitors coupled to a profound defect in astrogliogenesis, whereby HD astrocytes fail to express glial fibrillary acidic protein (GFAP). Mechanistically, this defect arises from dysregulation of an epigenetic regulatory axis involving EZH2 and LIN28 upregulation together with reduced expression of the mature let-7g microRNA. Epigenetic pharmacological interventions, targeting this pathway at distinct nodes—through EZH2 modulation, let-7g restoration, or LIN28 inhibition—rescued astroglial differentiation in human HD cells and improved motor function in a Drosophila HD model. Our findings suggest that mHTT might trigger a dual-phase astroglial failure: an early developmental impairment followed by a collapse of regenerative gliogenesis. This bimodal mechanism proposes astrocytic dysfunction as a central driver of HD pathogenesis. Finally, we identify a panel of clinically relevant epigenetic compounds that, by converging on distinct targets within this axis, hold promise for stage-spanning therapeutic strategies capable of modifying disease trajectory.

Cell Death & Differentiation; https://doi.org/10.1038/s41418-026-01812-8

INTRODUCTION

Huntington's disease (HD) is a progressive neurodegenerative disorder affecting motor [1], cognitive [2], and psychiatric [3] functions. Notably, clinical signs typically emerge years before neuroimaging and neuropathological abnormalities become detectable [4–10].

HD is caused by an expanded CAG trinucleotide repeat in the HTT gene (chromosome 4p16.3), with repeats exceeding 39 invariably leading to disease onset [11]. The resulting mutant protein (mHTT) interacts with over 350 cellular targets [12, 13], disrupting multiple cellular processes across various tissues, with the central nervous system (CNS) being the most profoundly affected. While multiple brain regions are involved, the basal ganglia, and particularly the medium spiny GABAergic neurons of the indirect pathway, undergo the most pronounced neurodegeneration [14–16].

[1]Cellular Reprogramming Unit, Neurological Disorders Research Group, Fondazione IRCCS Casa Sollievo Della Sofferenza, San Giovanni Rotondo, Italy. [2]UniCamillus University, Saint Camillus International University of Health Sciences, Rome, Italy. [3]School of Engineering Mathematics and Technology, University of Bristol, Bristol, UK. [4]NeuroEpigenetics Laboratory, Department of Cellular, Computational, and Integrative Biology - CIBIO, University of Trento, Trento, Italy. [5]Stemgen Spa, Milano, Italy. [6]Department of Biotechnology and Biosciences, University of Milano-Bicocca, Milan, Italy. [7]Advanced Therapies Production Unit, Fondazione IRCCS Casa Sollievo della Sofferenza, San Giovanni Rotondo, Italy. [8]Department of Biology and Biotechnologies "Charles Darwin", Sapienza University of Rome, Rome, Italy. [9]Laboratory of neurobiology and pathology, Department of Cellular, Computational and Integrative Biology-CIBIO, University of Trento, Trento, Italy. [10]Laboratorio d'Immunogenetica, Servizio di Medicina Trasfusionale, Fondazione IRCCS Casa Sollievo della Sofferenza, San Giovanni Rotondo, Italy. [11]Department of Physiology and Pharmacology, Sapienza University of Rome, Rome, Italy. [12]IRCCS Santa Lucia Foundation, Rome, Italy. [13]Hematopathology Unit, Fondazione IRCCS Casa Sollievo della Sofferenza, San Giovanni Rotondo, Italy. [14]Neurological Disorders Research Unit, Fondazione IRCCS-Casa Sollievo della Sofferenza, San Giovanni Rotondo, Italy. [15]Department of Science, Roma Tre University, Rome, Italy. [16]Biostructures and Biosystems National Institute (INBB), Roma, Italy. [17]Department of Drug Chemistry and Technologies, Sapienza University of Rome, Rome, Italy. [18]Cancer Stem Cells Unit, ISBReMIT, Fondazione IRCSS Casa Sollievo della Sofferenza, San Giovanni Rotondo, Italy. [19]Inborn Errors of Morphogenesis Research Unit, Section of Developmental Genomics, Fondazione IRCCS Casa Sollievo della Sofferenza, San Giovanni Rotondo, Italy. [20]Fondazione IRCCS Istituto Neurologico "C. Besta", Milano, Italy. [21]Huntington Disease Research Unit, Fondazione IRCCS Casa Sollievo della Sofferenza, San Giovanni Rotondo, Italy. [22]Center for Life Nano & Neuro Scienze CLN2S@Sapienza-Italian Institute of Technology (IIT), Rome, Italy. [23]Department of Biomedical Sciences (DBS), University of Padova, Padova, Italy. [24]Veneto Institute of Molecular Medicine (VIMM), Padova, Italy. [25]Department of Neurosurgery, University of Florida, Gainesville, FL, USA. [26]Faculty of Medicine, Link Campus University, Rome, Italy. [27]Abu Dhabi Stem Cell Centre, Abu Dhabi, United Arab Emirates. [28]These authors contributed equally: A. Casamassa, G. Ruotolo, AMG Giovenale. ✉email: j.rosati@operapadrepio.it; angelo.v@adscc.ae

Received: 7 October 2025 Accepted: 29 June 2026
Published online: 16 July 2026

Glial dysfunction is also a hallmark of HD. mHTT activates neuroinflammatory pathways—including NF-κB [17] and kynurenine signaling [18] leading to aberrant microglial activation and reactive astrogliosis [19]. Increasing evidence indicates that astrocytes contribute actively to HD pathogenesis, not only through reactive responses to neuronal injury but also through cell-autonomous alterations that impair metabolic support, synaptic regulation, and inflammatory signaling [20]. Astrocyte dysfunction contributes to glutamate-mediated excitotoxicity, as reduced expression of mainly the glutamate transporters GLAST and GLT-1 impairs glutamate clearance, resulting in elevated synaptic glutamate and overstimulation of NMDA and AMPA receptors in the striatum [21, 22].

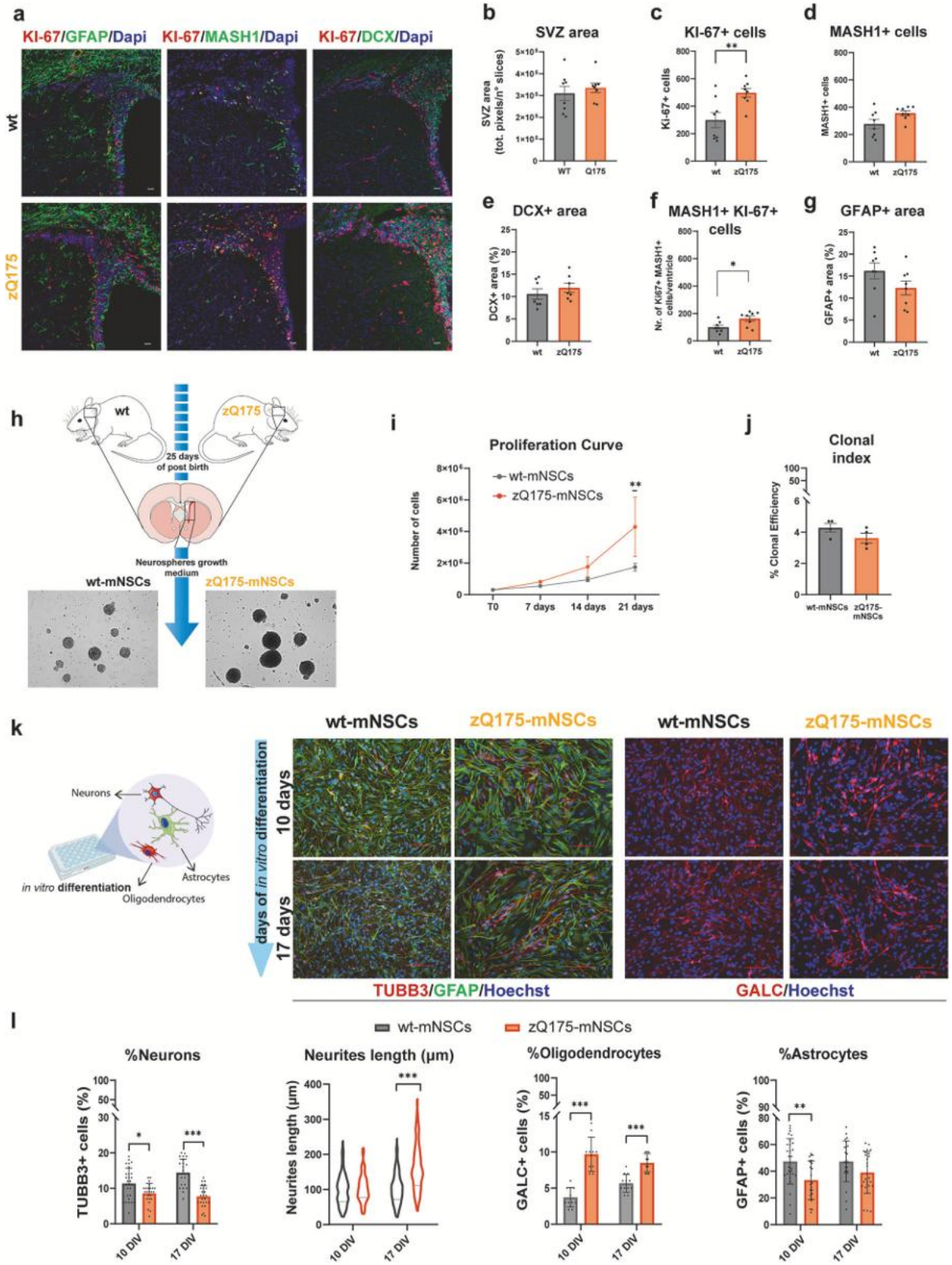


Fig. 1 zQ175 Mice Exhibit Early Neurogenic Niche Dysfunction and Impaired Neural Stem Cell Properties. a Representative fluorescent images showing KI-67 (red), GFAP (green), MASH1 (green), DCX (green), and DAPI (blue) staining in the RMS and SVZ of WT and zQ175 mice at post-natal day 7. Immunohistochemical analyses were performed on three separate litters. Scale bar: 20 μm. **b** SVZ area (total pixels/number of slices), **c** KI-67+ cells, **d** MASH1+ cells, **e** % of Doublecortin+ (DCX +) area, **f** MASH1 + KI-67+ cells, **g** % of GFAP+ area in zQ175 mice compared to WT mice. Each dot represents an individual mice ($n = 8$, except for DCX+ area, where $n = 7$). **h** Experimental scheme for mNSC line derivation from the SVZ of WT and zQ175 mice at post-natal day 25. **i** Number of viable WT- and zQ175-mNSCs after 7, 14, and 21 days of culture. **j** Clonal index of zQ175-mNSCs relative to WT-mNSCs, expressed as the percentage of clonal efficiency. All neurosphere experiments were performed in triplicate. **k** Experimental scheme (left) and representative immunofluorescence images (right) of spontaneous in vitro differentiation of WT- and zQ175-mNSCs into neurons (TUBB3+ cells, red), astrocytes (GFAP+ cells, green), and oligodendrocytes (GALC+ cells, red), 10 and 17 days after epidermal growth factor (EGF) removal. Scale bar: 100 μm. **l** % of neurons, neurite length (μm), % of oligodendrocytes, and % of astrocytes at 10 and 17 days of differentiation in zQ175-mNSC-derived neural cultures compared to WT cultures. Differentiation assays were performed in triplicate; for each biological replicate, 10 microscopy images per coverslip were analyzed. The reported values represent the median of image analyses from three independent experiments. In the image, dots correspond to one experiment for a line. zQ175 slices, zQ175-mNSCs, and differentiations are shown in orange, while the WT counterparts are in gray. All data are expressed as mean ± Standard Deviation (SD). Data were analyzed using unpaired Welch's t-test (**b–g**, $n = 8$; **j** $n = 4$), two-way ANOVA with Bonferroni's post hoc correction (**i**, $n = 3$), or Mann–Whitney U test (**l**). Statistical significance: $^{*}p \le 0.05$, $^{**}p \le 0.01$, $^{***}p \le 0.001$.

It is now evident that CNS damage begins decades before clinical onset [10, 23], with emerging evidence pointing to early developmental impairments. mHTT has been shown to disrupt neuronal migration [24, 25] and hinder oligodendrocyte maturation [26]. Even the earliest stages of neurodevelopment appear affected, including the activity of neural stem cells (NSCs) [27–29]. Supporting this, post-mortem analyses revealed an expansion of the subventricular zone (SVZ) - a region wherein NSCs reside in HD brains [30, 31]. In this perspective, early developmental disturbances affecting lineage specification might represent an underappreciated component in brain pathogenesis in HDs. In particular, defects arising precociously at the level of neural progenitors could establish subtle vulnerabilities in both neuronal and glial lineages that contribute to degeneration and disease progression throughout life. However, while neuronal developmental alterations have been investigated to some extent, the impact of mHTT on early astroglial development and astrogliogenesis remains comparatively poorly understood.

In this view and given the essential role of astrocytes in HD pathology and the limited knowledge on their developmental alterations in this disease, we sought to understand how mHTT alters neurogenesis, with particular attention to early neural precursors and astrogliogenesis.

Using NSCs from the zQ175 knock-in mouse model and from patient-derived iPSCs with various CAG repeat expansions (43, 64, 85), we observed increased proliferative activity in a subset of multipotent neural precursors and impaired astrocytic differentiation. Mechanistically, we found that both phenotypes arise from dysregulation of a central, tri-component molecular circuitry that underpins key epigenetic pathways. This phenomenon can be rescued pharmacologically, also in an in vivo Drosophila model of HD, highlighting a potential therapeutic axis to correct early developmental defects in HD.

RESULTS

SVZ-derived zQ175 NSCs expressing mHTT exhibit dysregulated self-renewal, increased proliferation, and altered differentiation

In postmortem brain specimens from HD patients, neurogenic regions such as the subgranular and subependymal zones of the hippocampus (SGZ/SGL) and lateral ventricles (SVZ/SEL) appear dysplastic and show increased cellular proliferation [30, 32]. Findings in rodent models have been more variable, likely due to differences in the developmental stages studied [28, 29, 33]. Therefore, data collected at more advanced stages of the disease may be influenced by neurodegenerative and inflammatory processes, which could obscure the primary effects of mHTT that appear earlier in disease progression.

To investigate early neurogenic alterations in HD, we analyzed the zQ175 knock-in mouse model, which expresses full-length mHTT with approximately 190 CAG repeats under the control of the endogenous mouse Htt promoter [34, 35]. Analyses were performed at postnatal day 7 (P7), a developmental stage in which no overt neurodegenerative signs are typically observed [36]. Using immunohistochemistry, confocal microscopy, and serial stack reconstruction, we identified a proliferation defect in the neural stem cell (NSC) niche of the subventricular zone (SVZ), consistent with alterations reported in postmortem human HD brains.

While overall SVZ area did not differ between wild-type (WT) and zQ175 mice (Fig. 1a, b), zQ175 brains exhibited a significantly higher number of proliferating (Ki67 +) cells (Fig. 1c). To identify the most affected SVZ populations, we quantified GFAP+ NSCs (Type B cells; Fig. 1g), MASH1+ (ASCL1 +) progenitors (transit amplifying Type C progenitors; Fig. 1d), and DCX+ neuroblasts (Type A cells; Fig. 1e). Of note, we observed a significant increase in proliferating MASH1+ cells (MASH1 + /Ki67 + ; Fig. 1f), while no significant changes were observed in the total numbers of MASH1+ cells (Fig. 1d), DCX+ area (Fig. 1e) and density of GFAP + NSCs (Fig. 1g).

These findings mirror alterations observed in neurogenic zones of HD patient brains [28], which were not consistently reported in earlier rodent models. Importantly, they suggest that dysregulation of neurogenesis is already detectable at early postnatal stages in HD, prior to the onset of neurodegeneration. Our data also support a model in which mHTT expression leads to early expansion of the transiently amplifying Type C progenitor pool, accompanied by an increase in neuroblasts and a modest reduction in the NSC astroglial population.

Based on our in vivo findings, we analyzed multipotent neural progenitor/stem cells (NSCs), isolated and cultured from the SVZ of the same mice (zQ175-mNSCs), and their progeny. Using the classical neurosphere culture system [37], we compared the proliferation, self-renewal and differentiation capacity of zQ175-mNSC, to wild-type, age, strain matched NSCs (WT-mNSC; Fig. 1h). We found that the overall proliferation of zQ175-mNSCs was significantly exacerbated (Fig. 1i) while their clonal efficiency remained unchanged (Fig. 1j). These data suggest that mHTT does not impact NSCs, instead it affects their immediately downstream cell lineage, namely the rapidly dividing, transient amplifying Type C progenitor cells. This aligns with the increase in dividing MASH1+ cells (Fig. 1f) observed in the zQ175 mouse SVZ.

We next assessed whether mHTT could also impinge on the differentiation process as recapitulated by culturing NSCs from WT- and zQ175-mNSCs, which were triggered to differentiate by growth factor removal [38]. We assessed the percentage of (1) neurons (and their neurite length; β-tubulin III positive cells, TUBB3 +); (2) astrocytes (glial fibrillary acidic protein positive cells;

GFAP +); and (3) oligodendrocytes (galactocerebroside-positive cells) (GALC +) that were generated under these conditions (Fig. 1k). First, we found that the overall number of neurons that were generated in zQ175-mNSCs cultures was significantly lower than in WT-mNSCs, while the neurite length of neuronal cells was increased in zQ175 cultures (Fig. 1l), which was in agreement with previous studies conducted in HD models [26, 39–41]. We also observed that the percentage of oligodendrocytes was significantly increased (Fig. 1l) [26, 42]. However, the most prominent phenomenon was a significant reduction in the number of the GFAP+ cells in the zQ175-mNSCs cultures after 10 days of differentiation (Fig. 1l).

Altogether, the findings on the zQ175-mouse strengthen the notion that mHTT interferes with the proliferation of neural progenitors at various stages of the hierarchical process of neurogenesis. In such a context, the disturbance of type C transit-amplifying progenitor proliferation and failure of astroglial differentiation emerge as prominent phenomena.

Expanded polyQ Huntingtin affects the morphology and proliferation of iPSC-derived hiNSCs

We sought to determine whether the phenotypes observed in zQ175-mNSCs were conserved in human NSCs. To this end, we employed virus- and feeder-free hiPSC lines reprogrammed from skin fibroblasts of three HD patients carrying 43 (HD-hiPSCs#1), 64 (HD-hiPSCs#2), and 85 (HD-hiPSCs#3) CAG repeats in the HTT gene [43–45], and compared them to age- and sex-matched control hiPSCs (CTR-hiPSCs#1, #2, #3; <35 CAG repeats) (Fig. 2a).

Embryoid bodies (hiEBs; Fig. 2b) were generated from these lines [46], and stable human neural stem cell lines (hiNSCs; Fig. 2c) were derived as previously described [47]. While no overt differences were detected between CTR and HD lines at the iPSC or hiEB stage (Fig. 2a, b), morphological analysis at the hiNSC stage revealed clear differences. Compared to control neurospheres, HD-hiNSCs displayed a heterogeneous population of normal-sized and enlarged spheres, often containing dense, dark intracellular inclusions (Fig. 2c, right panel). Consistently, quantitative morphological assessment showed that all HD-hiNSCs formed neurospheres with a significantly increased diameter compared to CTR-hiNSCs, within the same growth time window (Fig.2d). Accordingly, HD-hiNSC cultures exhibited a significantly higher number of Ki67+ proliferating cells (Fig. 2e) and expanded in number more rapidly than CTR-hiNSCs (Fig. 2f). Cell death (data not shown) and clonogenic index (Fig. 2g), however, remained unchanged. These findings mirror those observed in zQ175-mNSCs and indicate that both mouse and human HD-derived NSCs show enhanced proliferative capacity without an increase in multipotent precursor frequency. This suggests an intrinsic dysregulation in the pool of transient amplifying (type C) progenitors [48].

Upon differentiation, HD-hiNSCs exhibited lineage-specific defects analogous to those seen in zQ175 progeny. When analyzed at 10 and 17 days in vitro (DIV) following growth factor withdrawal (Fig. 3a, b), HD-hiNSCs generated significantly fewer TUBB3+ neurons than CTR-hiNSCs (Fig. 3c). Moreover, CTR-derived neurons extended neurites in a uniform and radially dispersed pattern, whereas HD-hiNSC-derived neurons formed aberrant three-dimensional clusters with disorganized neurite outgrowth, evident by 10 DIV and persisting through 17 DIV (Fig. 3b, c). In parallel, the proportion of oligodendrocytes (GALC +) was significantly elevated in HD-hiNSC cultures compared to controls (Fig. 3b, c). Most notably, a marked reduction in the percentage of GFAP+ astrocytes was observed in HD-hiNSCs from all three patient lines at both 10 and 17 DIV. Specifically, at 10 DIV, GFAP+ cells accounted for 50.1% in CTR-hiNSCs versus 16.7%, 31.9%, and 16.5% in HD-hiNSCs; at 17 DIV, these values were 54.0% in controls versus 25.1%, 27.9%, and 25.1% in HD-hiNSCs (Fig. 3c).

Confocal microscopy confirmed a significantly lower number of GFAP+ cells in differentiated HD-hiNSC cultures compared to CTR-hiNSCs (Fig. 3d). This substantial reduction in GFAP expression was further validated by western blotting (Fig. 3e) and qRT-PCR (Fig. 3f).

Notably, this decline was accompanied by an increase in extracellular glutamate levels in HD-hiNSC cultures relative to CTR-hiNSCs; however, this difference did not reach statistical significance (Supplementary Fig. 1a). Given this trend, we further investigated the underlying mechanism using transcriptomic data. This analysis revealed a significant downregulation of EAAT2 (SLC1A2 gene, Bonferroni $p = 3.9\times 10^{-10}$), the major glutamate transporter involved in extracellular glutamate clearance, in HD-hiNSCs (Supplementary Table 1). Although not a direct functional demonstration, this finding is consistent with the trend observed in the glutamate measurements and supports the hypothesis that glutamate homeostasis is altered in HD-hiNSCs. To determine whether the alteration extended beyond GFAP and involved a broader defect in astrocytic lineage progression, we also examined additional astrocyte-related markers in the transcriptomic dataset. Both SOX9 and S100β were significantly downregulated in HD-hiNSCs (Supplementary Table. 1), further supporting an impairment in astrocytic lineage progression and/or maturation. In addition, we assessed vimentin expression, which is a marker of immature astrocytes. It was not differentially expressed in the transcriptomic analysis, and qRT-PCR confirmed comparable expression levels between HD and CTR hiNSCs (Data not shown). The astroglial differentiation impairment was not attributable to ex vivo conditions, as it was also observed in vivo following transplantation into the striatum of adult immunodeficient nude mice. Two weeks after stereotactic injection of 3×10^5 HD-hiNSCs or CTR-hiNSCs, we evaluated engraftment and astrocyte differentiation using an anti-human GFAP antibody (Supplementary Fig. 1b). HD-hiNSCs successfully engrafted but failed to produce the abundant GFAP+ astrocytes observed in CTR-hiNSC grafts.

Global transcriptomic profiling of HD-hiNSCs and CTR-hiNSCs using HTA-Chip arrays confirmed that significant and consistent molecular alterations underlie the astroglial phenotype in HD. Principal component analysis (PCA) revealed a clear separation between HD and CTR transcriptomes (Supplementary Fig. 1c). Differential expression (DE) analysis identified 871 significantly dysregulated genes (Bonferroni $p < 0.05$) out of 17,677 expressed coding genes—488 upregulated and 383 downregulated in HD-hiNSCs compared to controls (Supplementary Fig. 1d; Supplementary Table 1).

Gene ontology (GO-BP) and Reactome pathway enrichment analysis showed that downregulated genes were significantly associated with neural development (adjusted $p < 0.001$), while upregulated genes were enriched in pathways related to catabolism and hydrolysis (adjusted $p < 0.001$) (Supplementary Fig. 1e, f). Notably, genes involved in astrocyte and oligodendrocyte precursor (OPC) development were profoundly downregulated in HD-hiNSCs (astrocytes: Bonferroni $p = 1.56 \times 10^{-32}$; OPCs: Bonferroni $p = 5.03 \times 10^{-32}$) (Supplementary Table 2). Further analysis revealed significant enrichment of downregulated genes corresponding to AST2, AST5, and AST6 astrocyte populations, as defined by Su and collaborators [49], which are implicated in gliogenesis and synaptic regulation (AST5: Bonferroni-adjusted $p = 2 \times 10^{-10}$; AST2: $p = 16 \times 10^{-8}$; AST6: $p = 1.3 \times 10^{-4}$) (Supplementary Fig. 1d). These results confirm a defective astrogliogenic transcriptional program in HD-hiNSCs.

To test whether expression of mHTT alone could recapitulate these phenotypes, we transduced CTR-hiNSCs with lentiviral vectors encoding either wild-type human N-terminal HTT (pCAG 17Q HTT-N548, referred to as 17Q-hiNSC) or mutant N-terminal HTT with 73 CAG repeats (pCAG 73Q HTT-N548, referred to as

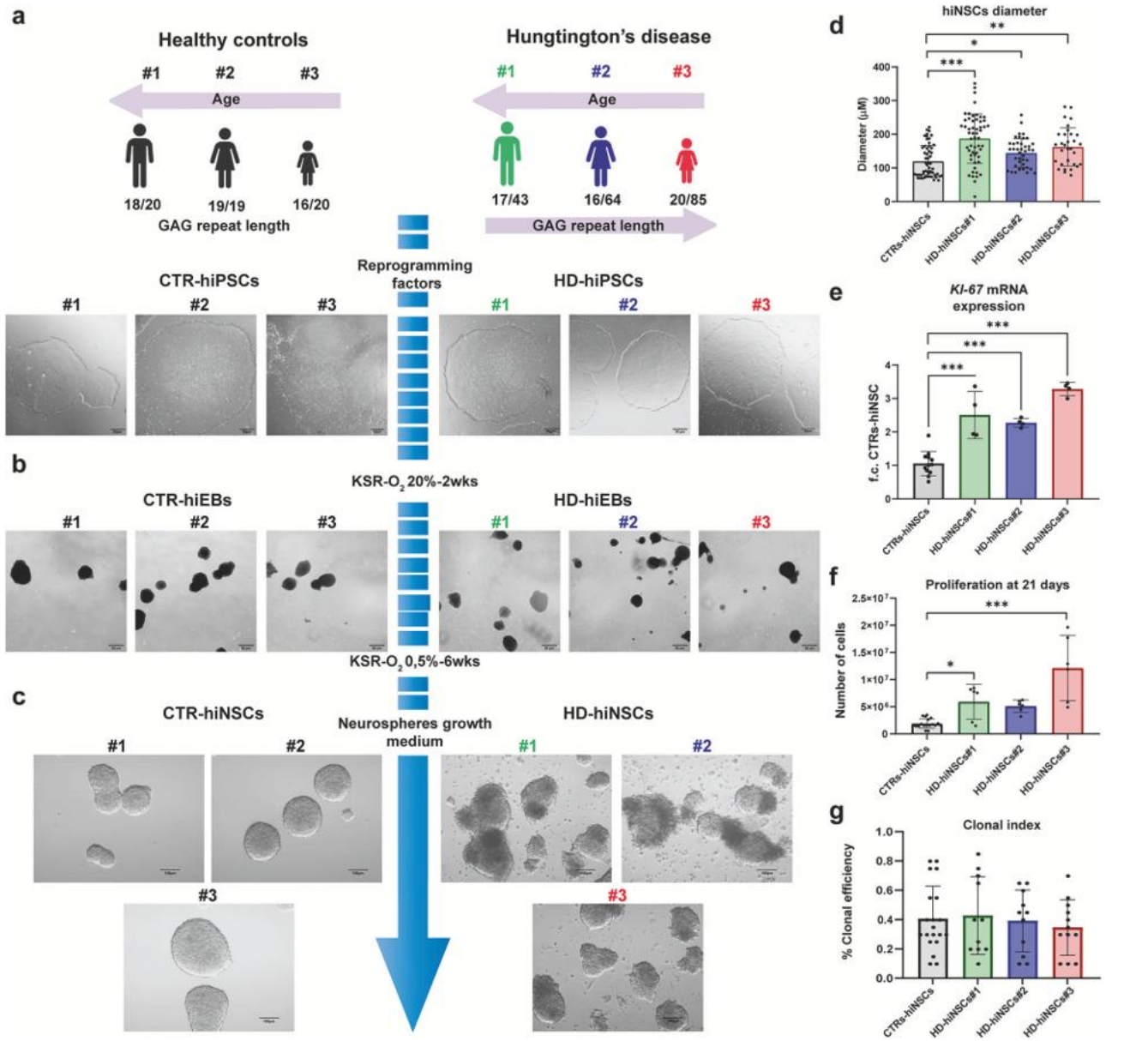


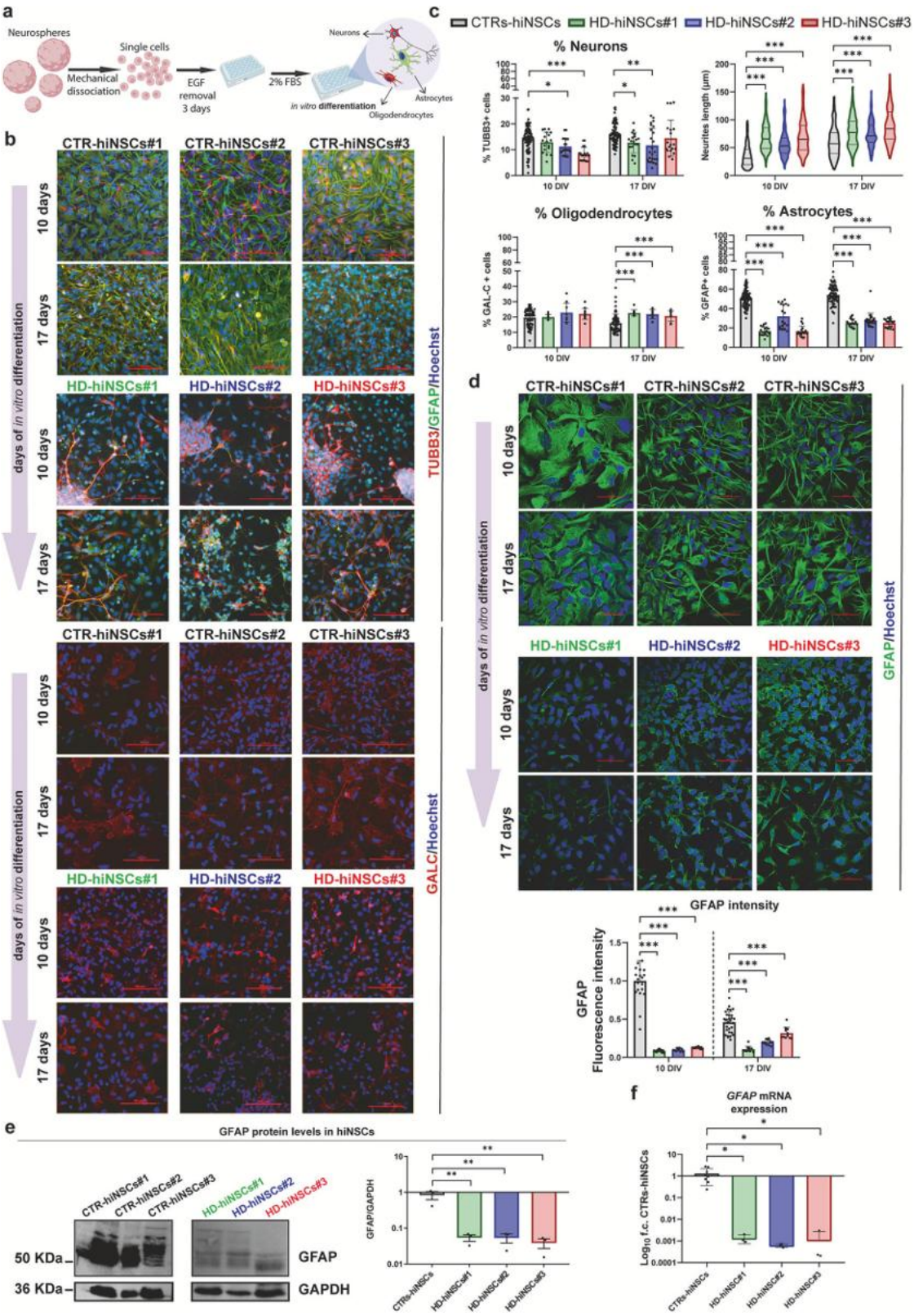
Fig. 2 Patient-Derived hiNSCs Reveal Early Neural Stem Cell Defects in Huntington's Disease. a Experimental outline for the derivation of hiPSC lines from fibroblasts of three HD patients with 43 (HD-hiPSCs#1, green), 64 (HD-hiPSCs#2, blue), and 85 (HD-hiPSCs#3, red) CAG repeats in the HTT gene, alongside hiPSCs derived from three healthy, age- and sex-matched controls (CTR-hiPSCs#1, #2, #3). Scale bar: 50 µm. **b** Morphological characteristics of hiPSC-derived Embryoid Bodies (hiEBs) cultured in KOSR medium for 52 days. Scale bar: 50 µm. **c** Morphological appearance of CTR and HD hiNSCs following transition to neurosphere growth medium. After multiple passages, CTR-hiNSCs formed well-defined, round, and clear neurosphere-like clusters, while HD-hiNSCs developed neurosphere-like clusters from darker, rounder structures with unclear boundaries. Scale bar: 100 µm. **d** Measure of CTR and HD hiNSCs diameters. Each dot represents the diameter of a single neurosphere. For each experiment around 10 neurospheres were analyzed. **e** qRT-PCR analysis of KI-67 gene transcript levels in HD (HD-hiNSCs#1, green; HD-hiNSCs#2, blue; HD-hiNSCs#3, red) compared to CTR-hiNSCs (mean of CTR#1, #2, #3, gray). **f** Viable cell counts of CTR and HD hiNSCs in neurosphere growth medium, measured after 21 days of culture. **g** Percentage of clonal efficiency in CTR and HD hiNSC lines. Each dot represents the percentage of neurospheres (50-100 µm in diameter) formed out of the total number of single-cell plates in a well. All data are presented as mean ± Standard Deviation (SD). Statistical analyses were performed using GraphPad Prism 8. Data were analyzed using Kruskal-Wallis test with Dunn's correction (**d**, $n = 3$) and one-way ANOVA with Bonferroni's post hoc correction (**e**, $n = 4$; **f**, $n = 6$; **g**, $n = 11$). Statistical significance: $^{*}p \leq 0.05$, $^{**}p \leq 0.01$, $^{***}p \leq 0.001$.

73Q-hiNSC), both under the synapsin I promoter [50, 51]. Transduction efficiency was monitored through qRT-PCR and western blotting (Supplementary Fig. 1h). Similar to HD-hiNSCs and zQ175-mNSCs, 73Q-hiNSCs exhibited accelerated proliferation compared to controls (Supplementary Fig. 1i). Notably, GFAP mRNA expression and protein content were significantly reduced in 73Q-hiNSCs (Supplementary Fig. 1j, k).

These results indicate that mHTT affects the activity of neuronal precursors and their progeny as observed in both murine and human models of HD.

Upregulation of the epigenetic effector EZH2 in HD NSCs

The polycomb repressive complex 2 (PRC2) subunit EZH2 regulates neural progenitor proliferation through deposition of



H3K27me3, a repressive histone mark that silences differentiation genes and helps maintain progenitor identity. Given that EZH2 enzymatic activity is enhanced by mutant huntingtin (mHTT) [52], and that EZH2 represses the GFAP promoter via H3K27me3-mediated silencing [53] - two mechanisms potentially underlying the disturbances observed in both mouse and human HD NSCs—we examined EZH2 expression in these cells to explore a possible mechanistic link to the observed phenotypes.

We found that EZH2 transcript levels were significantly increased in both HD-hiNSCs and zQ175-mNSCs (Fig. 4a and

Fig. 3 Aberrant Astrocytic Differentiation in Huntington's Disease hiPSC-Derived Neural Stem Cells. a Schematic diagram outlining the differentiation process of hiNSCs into specific neural cell types. Neurospheres were mechanically dissociated into single cells, then cultured for three days in a 24-well microplate without EGF. Subsequently, cells were placed in a medium (+2% FBS) to allow for spontaneous in vitro differentiation into neurons, astrocytes, and oligodendrocytes. **b** Representative immunofluorescence images depicting hiNSC-derived neurons (TUBB3+ cells, red), astrocytes (GFAP+ cells, green), and oligodendrocytes (GALC+ cells, red) from CTR#1, #2, #3 (black) and HD lines (HD-hiNSCs#1, green; HD-hiNSCs#2, blue; HD-hiNSCs#3, red) at 10 and 17 days post-EGF removal. Scale bar: 100 μm. **c** Quantification of neuronal percentage, neurite length (μm), oligodendrocyte, and astrocyte populations at 10 and 17 days of differentiation in neural cultures derived from CTR and HD-hiNSCs. Differentiation assays were performed in triplicate; for each biological replicate, 7 microscopy images per coverslip were analyzed. Reported values are medians from three independent experiments. Gray bars represent the mean across three replicates per CTR line (9 total). Dots indicate individual experiments per line. **d** Representative confocal images show GFAP$^+$ astrocytes (green) from CTR and HD hiNSCs. Scale bar: 50 μm. Below: GFAP fluorescence intensity in HD lines compared to the CTR mean (gray; CTR#1–3) at days 10 and 17 of differentiation. Analyses were done in triplicate; 3 images per coverslip per replicate. Values represent the median from three independent experiments. Gray bars show the mean across replicates per CTR line (9 total); dots represent single experiments per line. **e** Representative chemiluminescent western blot (left) shows GFAP and GAPDH expression across all lines. Densitometric analysis (right) compares GFAP/GAPDH levels in CTR vs. HD hiNSCs. Blots were performed in triplicate. All samples were loaded onto the same membrane and run simultaneously. For optimal signal detection, the membrane was cut and sections exposed separately: 5 s for CTR, 5 min for HD. **f** qRT-PCR analysis of GFAP gene transcript levels in all CTR and HD lines, normalized to the mean of CTR-hiNSCs. qRT-PCR analysis was performed in three biological replicates. Note: CTR values represent the average of the three control lines. All data are presented as mean ± Standard Deviation (SD). Statistical analyses were carried out using GraphPad Prism 8. Data were analyzed using Kruskal–Wallis test followed by Dunn's multiple-comparison test (**c**), one-way ANOVA with Bonferroni's post-hoc correction (d, $n = 11$; **f**, $n = 3$), or unpaired Welch's t-test (**e**, $n = 3$). Statistical significance: $^*p \le 0.05$, $^{**}p \le 0.01$, $^{***}p \le 0.001$.

Supplementary Fig. 1l, respectively). This upregulation was accompanied by elevated EZH2 protein levels in both mice (4-fold; Supplementary Fig. 1l) and human (2.5–3.5-fold; Fig. 4b) HD NSCs. Enhanced enzymatic activity was confirmed in the latter (Fig. 4c). A similar effect was reproduced by exogenous expression of mHTT in hiNSCs (73Q-hiNSCs), which led to increased EZH2 mRNA (Fig. 4d) and protein (Fig. 4e) levels compared to control 17Q-hiNSCs.

Notably, a ChIP-qPCR analysis of two regions within the GFAP promoter revealed a significant H3K27me3 enrichment at the –4.6 kb site in HD-hiNSCs#2 and #3 (Fig. 4f, above), indicating increased deposition of the repressive histone mark H3K27me3 at the GFAP promoter in HD-hiNSCs. To directly assess EZH2 occupancy at the GFAP locus, we also performed EZH2 ChIP–qPCR in our hiNSC model (Fig.4f, below). EZH2 was significantly enriched at both the proximal promoter and the −4.6 kb regulatory region in HD-hiNSCs compared with controls, indicating direct recruitment of EZH2 to GFAP regulatory elements in this disease context. These findings support the notion that increased EZH2 activity - driven by a gain-of-function interaction with mHTT [51] -represents a key molecular mechanism underlying both the aberrant proliferative behavior of multipotent neural progenitors and the impaired astroglial differentiation observed in both mouse and human HD NSCs (Fig. 4g).

Inhibition of EZH2 does not affect self-renewal but impacts proliferation and astroglial differentiation

To test whether EZH2 overactivation plays a causal role in the phenotypes observed in HD neural cells, we pharmacologically reduced EZH2 catalytic activity in both HD-hiNSCs and CTR-hiNSCs using two distinct chemical inhibitors: the FDA-approved Tazemetostat (TAZ) [54–57] and MS1943 [58]. These compounds operate through different mechanisms: TAZ inhibits EZH2's methyltransferase activity, thereby preventing H3K27me3 accumulation by PRC2, while MS1943 is a selective degrader that effectively reduces EZH2 protein levels, thus inhibiting the residual enzymatic activity. The Tazemetostat dose was selected based on previous studies reporting effective concentrations ranging from 1 to 5 μM with treatment durations of 7–16 days [54–57]. We therefore used 1 μM, as this concentration produced comparable inhibition of H3K27me3 in both CTRL and HD cells (Supplementary Fig. 2a) while significantly reducing cell proliferation without inducing detectable cell death (Supplementary Fig. 2d, f). For MS1943, we selected a low concentration of 100 nM, despite previous studies commonly using 5 μM [58]. Although the higher dose efficiently promoted EZH2 degradation (Supplementary Fig. 2b), it also induced marked toxicity, as evidenced by the presence of pyknotic nuclei (Supplementary Fig. 2c). In contrast, treatment with 100 nM MS1943 reduced cell proliferation while preserving cell viability (Supplementary Fig. 2e, g). Importantly, neither compound altered clonal efficiency (Supplementary Fig. 2h), indicating that self-renewal was not impacted.

Critically, when EZH2 inhibitors were applied at the onset of spontaneous differentiation, triggered by growth factor withdrawal (Fig. 5a), both TAZ and MS1943 led to increased GFAP expression and rescued the blunted astroglial phenotype observed in HD-hiNSC cultures (Fig. 5b, c), with confirmation by western blotting (Fig. 5d).

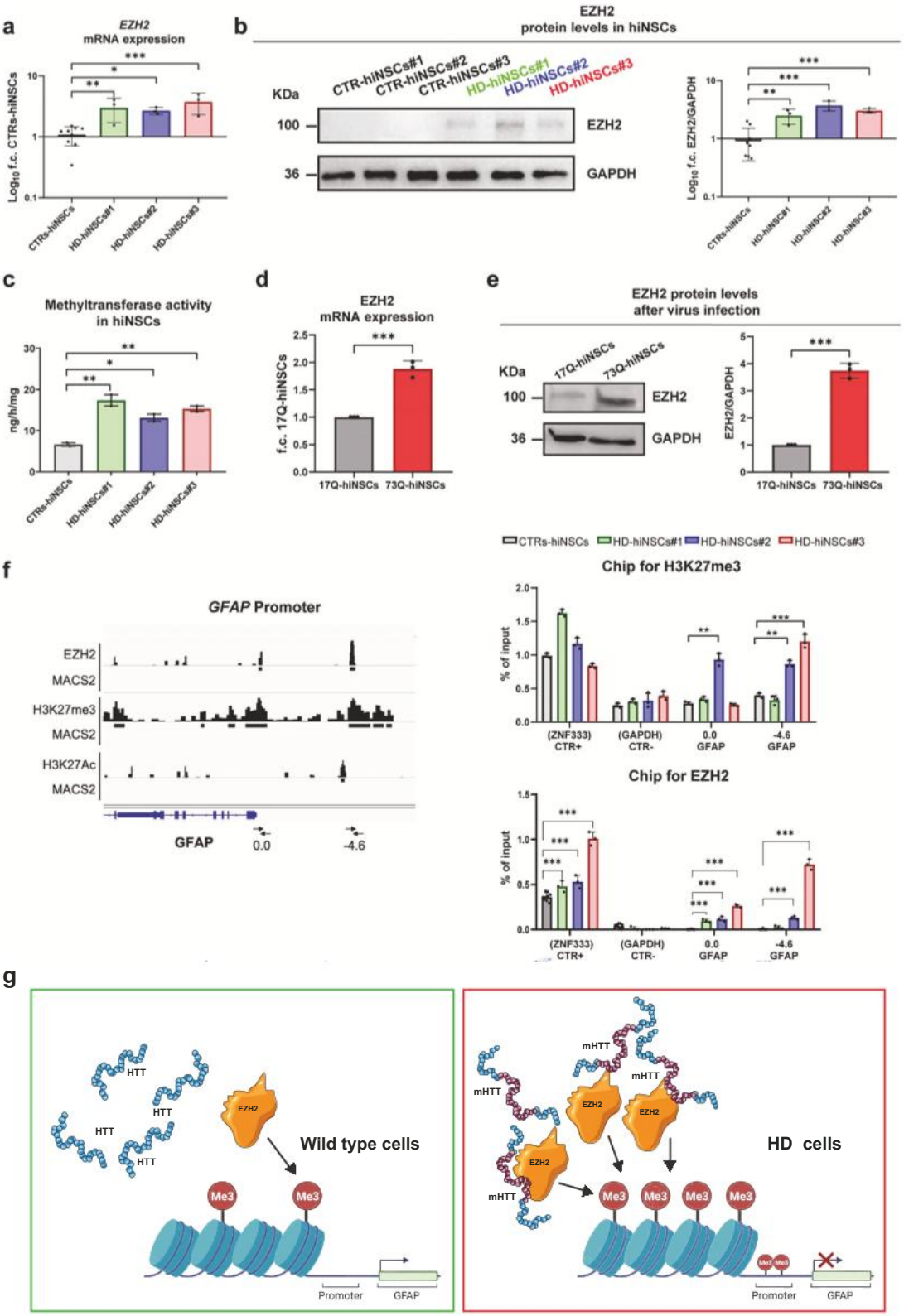
These findings demonstrate that EZH2 plays a central regulatory role in the neurogenic-to-gliogenic switch, and that its pathological upregulation in HD-hiNSCs underlies the aberrant proliferative expansion and impaired astroglial differentiation. Pharmacological inhibition of EZH2 is sufficient to rescue both phenotypes, supporting a causal role for EZH2 hyperactivity in the developmental defects observed in HD.

LIN28 is upregulated in HD-hiNSCs and impairs Let-7g maturation, sustaining EZH2 mRNA levels

To elucidate the mechanisms underlying the elevated EZH2 transcript levels in HD-hiNSCs, we investigated the regulation of EZH2 by the Let-7 microRNA family, known to bind and degrade EZH2 mRNA [59]. Although pri-let-7g levels were comparable between HD-hiNSCs and CTR-hiNSCs, qRT-PCR revealed a significant reduction in mature Let-7g in HD-hiNSCs (Fig. 6a). In contrast, mature let-7g levels remained unchanged between zQ175-mNSCs and WT-mNSCs, despite a significant increase in pri-let-7g in zQ175-mNSCs (Supplementary Fig. 3a), suggesting a human-specific or context-dependent alteration.

LIN28, a well-known inhibitor of Let-7 processing, tightly controls Let-7 maturation. Notably, both Lin28 mRNA and LIN28 protein were significantly upregulated in HD-hiNSCs and zQ175-mNSCs compared to controls (Fig. 6a, b and Supplementary Fig. 3b), indicating that excess LIN28 may block Let-7g maturation in HD neural progenitors.

Altogether, these findings support a regulatory cascade in which LIN28 upregulation in HD-hiNSCs impairs Let-7g maturation, leading to stabilization of EZH2 mRNA and its overexpression. The resulting elevation in EZH2 would promote the increased proliferation and impaired astroglial differentiation characteristic of HD-hiNSCs. To functionally test this hypothesis, we pharmacologically restored Let-7g activity using two compounds that target different steps of the Let-7–LIN28 axis: (1) IPA3, a terminal uridine



transferase (TUTase) inhibitor, blocks pre-let-7 uridylation and degradation by the DIS3L2 exonuclease, thereby enhancing Let-7 maturation [60, 61]; (2) 1632 (N-methyl-N-[3-(3-methyl[1,2,4] triazolo[4,3-b]pyridazin-6-yl)phenyl]acetamide), an inhibitor of LIN28/pre-let-7 binding, disrupts LIN28-mediated repression of Let-7 processing [62] (Fig. 6c). We screened three IPA-3 concentrations (10 nM, 100 nM, 1 μM) and assessed their ability to increase let-7 expression. The lowest effective dose (10 nM) was selected to limit potential toxicity (Supplementary Fig. 3c). Compound 1632 is typically used at ≥20 μM, but in our experiments, we employed the minimal effective concentration (0.6 μM) to further reduce toxic effects (Supplementary Fig. 3c).

Fig. 4 Enhanced EZH2 Activity Links Mutant Huntingtin to GFAP Transcriptional Repression. a qRT-PCR analysis of EZH2 gene transcript levels in HD-hiNSC lines (HD-hiNSCs#1, green; HD-hiNSCs#2, blue; HD-hiNSCs#3, red), normalized to the CTR-hiNSC lines (mean of CTR#1, #2, #3, gray). **b** On the left, a representative chemiluminescent western blot showing the molecular weights and protein levels of EZH2 and GAPDH across all analyzed lines. For clarity, lanes from the same western blot were rearranged in the figure. The complete uncropped blot is shown in Supplementary Figure "Uncropped western blots". No image content was added, removed, or digitally altered. On the right, densitometry analysis of EZH2/GAPDH expression comparing CTR- vs. HD-hiNSCs. **c** Measurement of Histone Methyltransferase (H3-K27) activity (ng/h/mg) in HD-hiNSCs vs CTRs. **d** Following viral infection, qRT-PCR was used to measure EZH2 mRNA expression in CTR-hiNSCs, with the expression levels in 73Q cells compared to those in 17Q-hiNSCs for normalization. **e** Western Blot analysis of EZH2 protein expression in 73Q-hiNSCs vs. 17Q-hiNSCs and its densitometry. **f** GFAP promoter analysis of H3K27me3 (left) and ChIP results (right) showing H3K27me3 modifications in two regions of the GFAP promoter. **g** Hypothetical pathogenic mechanism of HD vs. wild-type cells, linking mutant HTT (mHTT) with EZH2 overexpression and subsequent repression of the GFAP promoter. All experiments were performed in triplicate, except for panel a, which was performed in quadruplicate. Data are presented as mean ± Standard Deviation (SD). Statistical analyses were carried out using GraphPad Prism 8. Data were analyzed using one-way ANOVA with Bonferroni's post hoc correction (**a–c**, $n = 3$), unpaired t-test (**d, e**, $n = 3$), or two-way ANOVA with Bonferroni's post hoc correction (**f**, $n = 3$). Statistical significance: $^{*}p \leq 0.05$, $^{**}p \leq 0.01$, $^{***}p \leq 0.001$.

Both IPA-3 and 1632 were administered during prolonged treatment.

At non-toxic and effective doses (IPA3: 10 nM [63]; 1632: 0.6 µM; Supplementary Fig. 3c–h), both compounds reduced proliferation in HD-hiNSCs, without affecting cell viability or clonogenic potential (Supplementary Fig. 3d–h), except in HD-hiNSC#2. Importantly, both IPA3 and 1632 restored GFAP expression in the previously nearly GFAP-negative astroglial progeny of HD-hiNSCs (Fig. 6d–f), confirming functional rescue of astrocytic differentiation.

These data reinforce the model whereby LIN28-mediated suppression of Let-7g contributes to EZH2 overexpression, thereby linking altered post-transcriptional regulation to aberrant lineage progression in HD neural stem cells.

Epigenetic modulators improve motor function in a Drosophila model of Huntington's disease

Drosophila models are powerful tools for investigating in vivo pharmacological modulation of neurodegenerative diseases, including Huntington's disease (HD). In this study, we leveraged the Drosophila HD model developed by Botas and colleagues [64], which recapitulates key pathological features of the human disorder and provides a robust platform to dissect neurodegenerative mechanisms and evaluate therapeutic candidates.

This model expresses full-length human huntingtin (Htt) with either 16 (16QHtt, wild-type) or 128 (128QHtt, mutant) glutamine repeats under control of the UAS promoter system. Upon crossing with elav-Gal4 drivers, which induce pan-neuronal expression from early developmental stages [65], the transgenic progeny exhibit spatially and temporally regulated mHTT expression. This model was chosen to take advantage of its proven utility for studying drug-based modifiers of HD neurodegeneration [66–73]. Consistent with our in vitro findings, HD flies (128QHtt) showed upregulation of both Ezh2 and Lin28 transcripts (Fig. 7a), providing a rationale to test the therapeutic impact of pharmacological inhibitors targeting these pathways. To assess the neuroprotective and therapeutic potential of epigenetic drugs in vivo, we measured the locomotor performance of HD (elav-Gal4 > 128QHtt) and control (elav-Gal4 > 16QHtt) flies fed standard media supplemented with Tazemetostat (TAZ; 50 µM), MS1943 (20 µM), IPA3 (10 µM), and 1632 (50 µM), throughout development.

Climbing ability was evaluated 6–7 days post-eclosion and compared to HD flies treated with vehicle (DMSO). As expected, no significant changes were observed in control flies (*elav-Gal4 > 16QHtt*; 16Q) across treatment groups (Fig. 7b). In contrast, HD flies (*elav-Gal4 > 128QHtt*, 128Q) showed a significant improvement in climbing behavior upon treatment with all four compounds (Fig. 7c). Given that climbing ability in Drosophila is a validated proxy for neurodegeneration [74], these results indicate that epigenetic drug administration effectively ameliorates mHTT-induced motor deficits in vivo.

Notably, these inhibitors did not significantly impact the motor performance of control animals expressing the non-pathological Htt variant (16QHtt), highlighting their selective efficacy in targeting HD-related neurodegenerative processes while preserving normal motor function.

In summary, the data support a mechanistic model (illustrated and extended in Fig. 7d) in which mutant huntingtin (mHTT) disrupts neurodevelopmental programs by promoting the expansion of early multipotent neural progenitors and impairing their differentiation into astroglial cells. These effects are mediated, at least in part, by increased EZH2 activity, which arises from upregulation of LIN28 and the consequent inhibition of Let-7g microRNA maturation. Since Let-7g normally represses EZH2 mRNA, its downregulation leads to sustained EZH2 expression, enhancing H3K27me3-mediated repression of genes critical for astrocytic differentiation. Pharmacological interventions targeting this pathway, whether by inhibiting EZH2 enzymatic activity, destabilizing EZH2 protein, or enhancing Let-7g maturation, effectively restored proliferative capacity and astroglial differentiation in HD-hiNSCs. Notably, the therapeutic potential of targeting this epigenetic axis was further corroborated in vivo by improved motor performance in 128Q flies relative to 16Q controls. Collectively, these findings identify a novel and druggable epigenetic mechanism underlying mHTT-mediated neurodevelopmental defects in Huntington's disease.

DISCUSSION

By investigating neurogenesis in both transgenic Huntington's disease (HD) mouse models and HD iPSC-derived human induced neural stem cells (hiNSCs), we demonstrate that mutant huntingtin (mHTT) disrupts the functional integrity of multipotent neural progenitors, leading to excessive proliferation and concomitant impairment of astrogliogenesis. Consequently, both murine and human HD-derived astroglia fail to undergo proper maturation, exhibiting marked deficits in the expression of GFAP even upon orthotopic implantation. Our data indicate that this aberrant phenotype correlates with upregulation of EZH2 in HD cells. This, in turn, is associated with a reduction in let-7g microRNA levels—a regulatory molecule that under normal conditions promotes EZH2 mRNA degradation. Furthermore, decreased let-7g expression is linked to elevated levels of the LIN28 protein, which is known to act dually as a suppressor and target of let-7g [75]. Importantly, pharmacological modulation of the EZH2–let-7g–LIN28 axis not only mitigates aberrant neural progenitor proliferation but also restores GFAP expression in HD astroglia and ameliorates motor dysfunction in a *Drosophila melanogaster* transgenic HD model.

In neural cells, mHTT disrupts a broad spectrum of molecular and cellular processes that are critical for neurodevelopment and homeostasis [76, 77]. Notably, the impact of mHTT extends to early neurogenic events, thereby affecting the ontogeny of CNS macroglia [24, 25]. Aberrant proliferation and delayed maturation

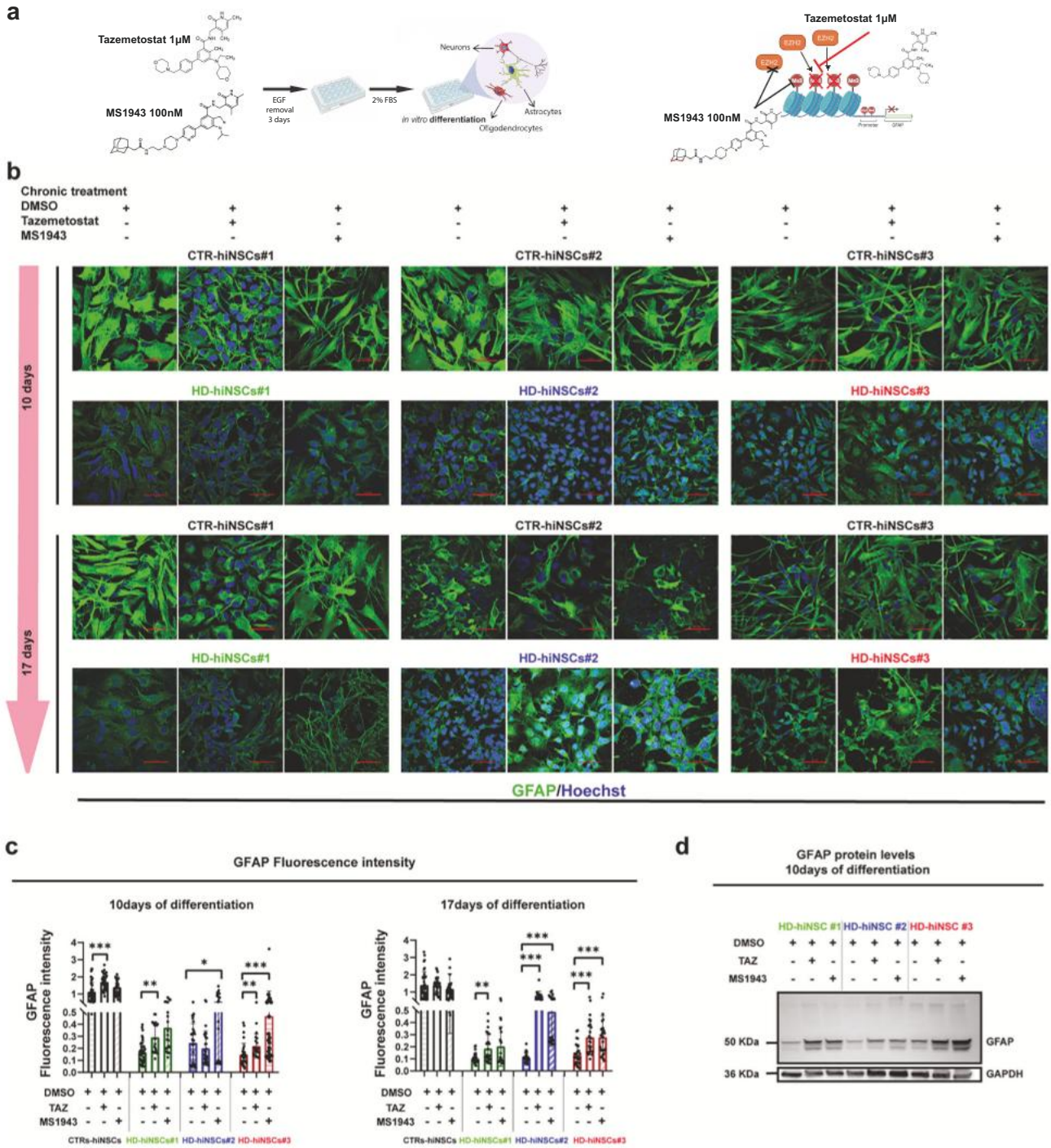
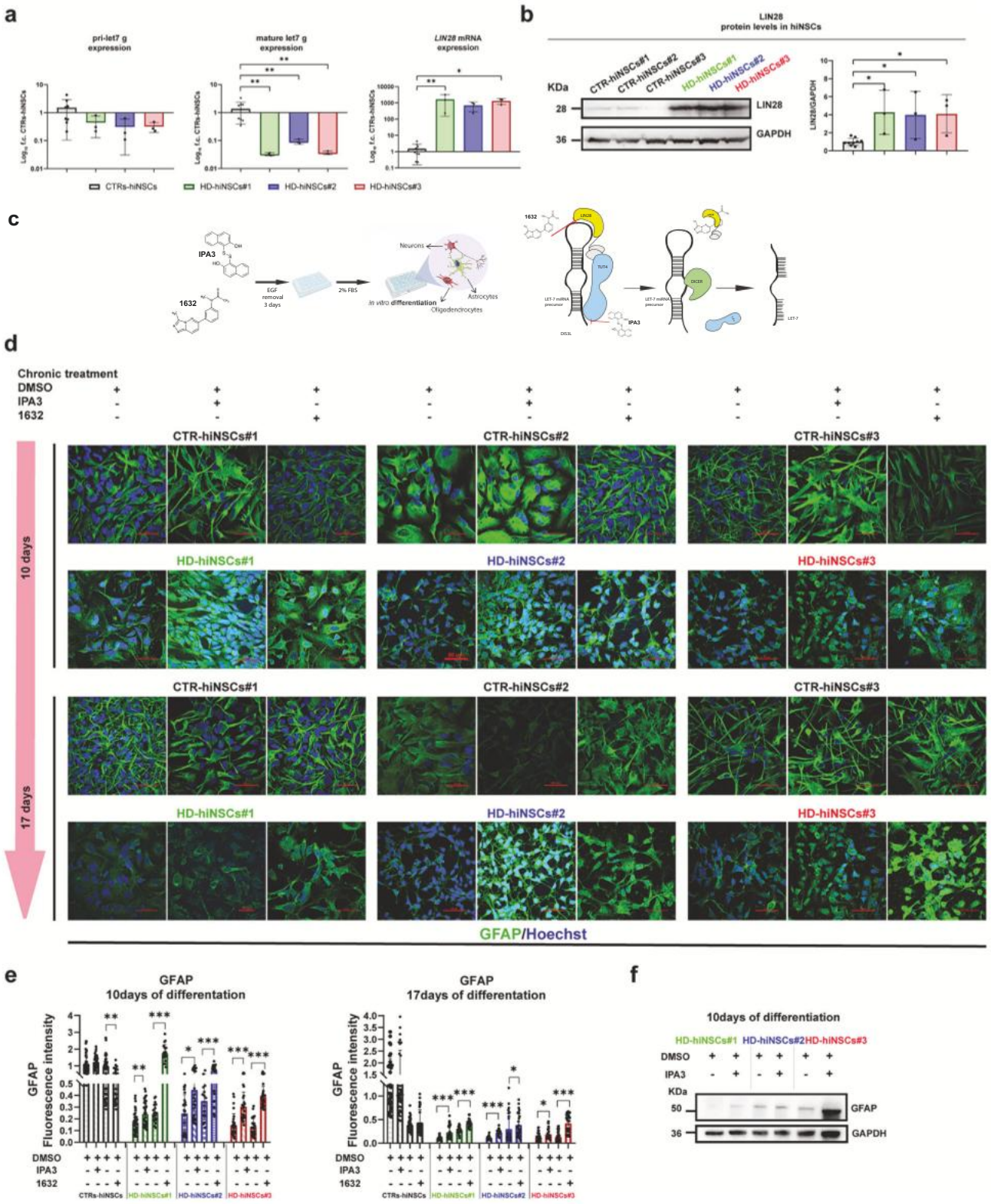


Fig. 5 Pharmacological Inhibition of EZH2 Restores GFAP Expression in Huntington's Disease hiNSCs. a The experimental treatment protocol, on the left and the mechanism of action of the two EZH2 repressors, Tazemetostat (1 μM) and MS1943 (100 nM), on the right. **b** Representative confocal images showing CTR#1, #2, #3 (black) and HD-hiNSC lines (HD-hiNSCs#1, green; HD-hiNSCs#2, blue; HD-hiNSCs#3, red) differentiated into astrocytes (GFAP+ cells, green, Hoechst + nuclei, blue) after 10 and 17 days of treatment with Tazemetostat, MS1943, or vehicle (DMSO). Scale bar: 50 μm. **c** Analysis of GFAP Fluorescence Intensity in the three HD lines compared to CTR lines (mean of CTR#1, #2, #3, gray) after 10 or 17 days of differentiation and treatments. GFAP analyses were performed in triplicate; for each biological replicate, 10 microscopy images per coverslip were analyzed. The reported values represent the median of image analyses from three independent experiments. Dots are representative of one experiment for line. **d** Western blot analysis of GFAP and GAPDH protein levels in HD-hiNSCs after 10 days of differentiation, treated with Tazemetostat (1 μM), MS1943 (100 nM), or DMSO. The experiment was performed in duplicate. All data are presented as mean ± Standard Deviation (SD). Statistical analyses were performed using GraphPad Prism 8. Data (c) were analyzed using the Kruskal–Wallis test followed by Dunn's multiple-comparison test. Statistical significance: $*p \leq 0.05$, $**p \leq 0.01$, $***p \leq 0.001$.



of oligodendroglial progenitors have been consistently reported in HD models [26, 78–80], along with a downregulation of glial lineage transcription factors in bipotent glial precursors and their impaired ability to effectively initiate myelination in hypomyelinated murine models [39]. Mature astrocytes in HD are similarly impaired, exhibiting profound alterations in gene expression profiles, morphological organization, and key homeostatic and metabolic functions [20, 81]. Despite these findings, the effects of mHTT on early astrogliogenesis, as well as the underlying molecular mechanisms, remain incompletely characterized. Early investigations in rodent models of Huntington's disease (HD) did not detect significant alterations in astrocyte density within adult neurogenic niches. Similarly, astroglial differentiation from human induced pluripotent stem cells (iPSCs) derived from HD patients initially

Fig. 6 Pharmacological Modulation of the LIN28/let-7g Axis Restores GFAP Expression in Huntington's Disease hiNSCs. a qRT-PCR analysis of pri-let-7g, mature let-7g, and LIN28 mRNA expression in CTR-hiNSCs (average of CTR#1, #2, and #3, shown in gray) and HD-hiNSCs (HD-hiNSC#1 in green, HD-hiNSC#2 in blue, HD-hiNSC#3 in red). **b** Representative chemiluminescent Western blot (left) showing molecular weights and expression levels of LIN28 and GAPDH proteins across all analyzed lines. On the right, quantification of LIN28 protein normalized to GAPDH in CTR- vs. HD-hiNSCs. **c** Schematic representation of the experimental treatment protocol (left) and the proposed mechanisms of action for IPA3 (10 nM) and compound 1632 (0.6 μM) (right). **d** Representative confocal images of astrocytes derived from CTR#1, #2, #3 (shown in black) and HD-hiNSCs (HD-hiNSC#1 in green, HD-hiNSC#2 in blue, HD-hiNSC#3 in red) (GFAP-positive cells in green; nuclei counterstained with Hoechst in blue), after 10 and 17 days of differentiation and treatment with IPA3, 1632, or vehicle (DMSO). Scale bar: 50 μm. **e** Quantification of GFAP fluorescence intensity in HD-hiNSC lines compared to CTRs at 10 and 17 days of differentiation, following the indicated treatments. GFAP analyses were performed in triplicate; for each biological replicate, 10 microscopy images per coverslip were analyzed. Dots are representative of one experiment for line. **f** Western blot analysis of GFAP and GAPDH protein levels in HD-hiNSCs after 10 days of differentiation with IPA3 (10 nM), 1632 (0.6 μM), or DMSO. All qRT-PCR analyses were carried out in at least three replicates. Western blot experiments were performed in triplicate. All data are presented as mean ± Standard Deviation (SD). Statistical analyses were performed using GraphPad Prism 8. Data were analyzed using one-way ANOVA with Bonferroni's post-hoc correction (**a, b**, $n = 3$) or Kruskal–Wallis test followed by Dunn's multiple-comparison test (**e**). Statistical significance: $^{*}p \leq 0.05$, $^{**}p \leq 0.01$, $^{***}p \leq 0.001$.

appeared unperturbed, showing no overt signs of dysfunction [82]. However, more recent evidence indicates that astrocytes derived from bipotent glial progenitors originating from HD embryonic stem cells exhibit an abnormal maturation trajectory, suggestive of disrupted developmental programming [39].

In this study, we first demonstrate that cultured multipotent neural stem and progenitor cells (NSCs) isolated from the subventricular zone (SVZ) of zQ175 Huntington's disease (HD) mice and HD patient-derived human induced NSCs (hiNSCs) exhibit significantly enhanced proliferative activity, along with a downregulation of genes critical for gliogenic lineage specification during development [49]. Consequently, these progenitor cells give rise to astrocytes that fail to express glial fibrillary acidic protein (GFAP) - a phenotype that was pronounced, persistent, and not reversible by orthotopic transplantation. Additionally, this deficit was recapitulated in wild-type hiNSCs after the forced expression of mHTT, reinforcing the idea that mHTT fundamentally disrupts gliogenic maturation pathways.

Together, these observations lay the groundwork for studying a mechanistic molecular model linking mHTT expression to altered neurogenesis - and more broadly, to disrupted neurodevelopment - which we further explored. Thus, a second key finding was the identification of the putative molecular targets dysregulated by mHTT in NSCs, which likely drove both their aberrant proliferative behavior and disruption of early astrogliogenesis. A critical event in this scenario was the marked upregulation of the transcription factor EZH2 in both mouse and human HD NSCs [14, 83]. EZH2 played a causal role in promoting enhanced NSCs proliferation and in suppressing GFAP expression in astroglial progeny [84]. In fact, by employing the histone lysine methylation inhibitor tazemetostat (TAZ) or selectively promoting EZH2 degradation with MS1943, we effectively counteracted both EZH2 activity and overexpression in HD cells, thereby rescuing the altered phenotype of HD-hiNSCs and mitigating their excessive proliferation, while also restoring GFAP expression in their astrocytic offspring.

Moreover, our mechanistic investigation led to a third significant finding: the overexpression of EZH2 in HD neural cells was associated with the deregulation of the Let-7/Lin28 regulatory axis. EZH2 degradation is known to be mediated by members of the Let-7 microRNA family, whose levels were significantly reduced in all neural cells expressing mHTT in our study. Restoring this pathway by enhancing Let-7 maturation with the uridylase inhibitor IPA3 increased let-7g levels and corrected both the aberrant proliferative behavior and the impaired astroglial differentiation. Similarly, the 1632 compound, which antagonizes Lin28 binding to pri- and pre-let-7 precursors, also increased let-7g levels, reduced hiNSC proliferation, and restored GFAP expression in their astrocytic progeny. Literature data support this scenario and lend support to the mechanistic model proposed in Fig. 7. According to this model, mHTT interferes with the degradation of β-catenin, resulting in toxic β-catenin accumulation [85]. This toxic buildup induces the upregulation of Lin28 and the downregulation of Let-7, also leading to the upregulation of EZH2 mRNA. Additionally, mHTT might directly stabilize the EZH2 protein, further enhancing its activity. EZH2 thus emerges as a key effector in this cascade, driving the excessive proliferation of NSCs and the defective astrogliogenesis in HD described here.

The cellular and molecular alterations, as well as the effects of the epigenetic treatments observed in this study, were largely consistent across patient-derived samples. A minor exception was noted in cells derived from patient 2, which did not exhibit corrected proliferative behavior in response to epigenetic drug treatment. However, astrogliogenesis was still successfully rescued in these cells. This discrepancy may be attributable to the patient's clinical background. At the time of biopsy, the patient had experienced a prolonged disease course of approximately 10 years and was in an advanced stage of clinical deterioration, passing away only a few months later. This advanced pathological context may have limited the capacity for pharmacological rescue of certain cellular phenotypes.

The findings discussed so far prompt relevant considerations regarding our understanding of HD pathogenesis and carry therapeutic implications that extend beyond current drug development strategies for this disease. As shown here, a hallmark of defective astrogliogenesis in our HD NSCs - namely, their failure to generate mature astroglia, as evidenced by persistently low GFAP expression - was both robust and long-lasting, even in vivo, upon transplantation. Yet, to our knowledge, no reduction in GFAP expression has been reported in HD patients or animal models, either during development or adulthood. This discrepancy raises important questions about the role and detectability of this phenomenon in the progression of HD.

Our findings raise the possibility that astroglial dysfunction in HD may originate during early developmental stages, establishing a latent vulnerability that precedes and potentially contributes to the astroglial changes observed in the adult diseased brain. Still, at first glance, our observations may appear inconsistent with the established neuropathological literature, where GFAP expression in HD brains is typically reported to be unchanged or increased at later disease stages and is widely interpreted as a hallmark of reactive astrogliosis [86–88].

A useful conceptual framework to reconcile these observations is provided by GFAP-deficient models. In these systems, early CNS development proceeds relatively normally due to compensatory expression of intermediate filament proteins other than GFAP, particularly vimentin [89–93]. However, this compensation is incomplete and, over time, leads to progressive astrocytic dysfunction, including alterations in cytoskeletal organization, mechanical resilience, and neural support functions [94, 95]. These findings indicate that precocious developmental deficits in GFAP

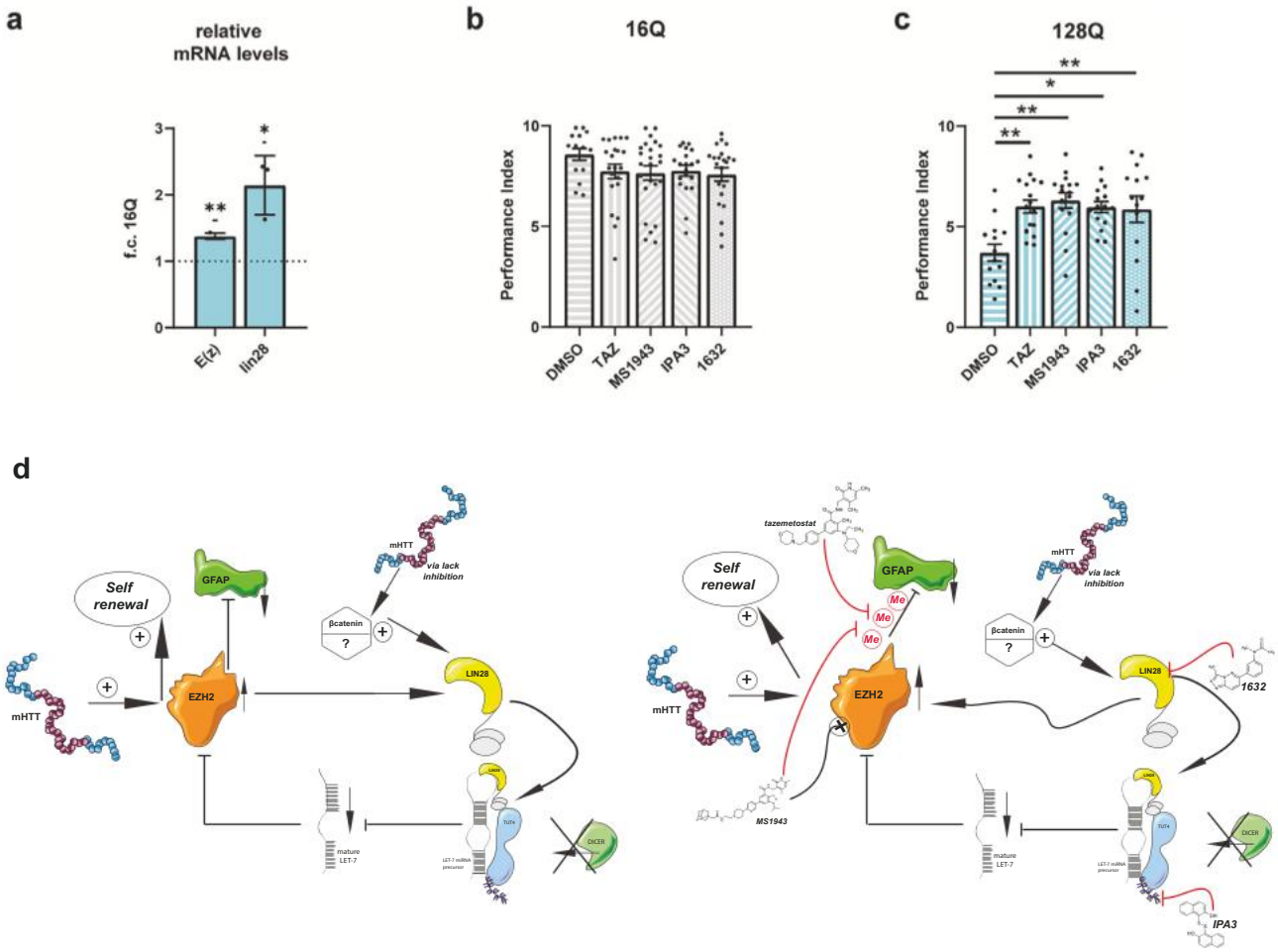


Fig. 7 In Vivo Validation of EZH2/LIN28 Dysregulation and Pharmacological Rescue in a Drosophila Model of Huntington's Disease. **a** qRT-PCR analysis of E(z) and lin28 expression in HD flies. Transcript levels of HD flies (elav-Gal4 > 128QHtt) were normalized to rp49 and displayed as fold change relative to control flies (elav-Gal4 > 16QHtt). Bar graph represents the mean ± SEM from three independent biological replicates (*$p < 0.05$, **$p < 0.01$, one-sample t-test). Black dots indicate individual data points, and the horizontal dotted line indicates the fold change control value, set to 1. **b** Climbing assay of control flies treated individually with TAZ, MS1943, IPA3, or 1632 during larval and adult stages. Black dots indicate individual data points from three independent biological replicates. **c** Climbing assay of HD flies treated individually with TAZ, MS1943, IPA3, or 1632 during larval and adult stages. Black dots indicate individual data points from three independent biological replicates. **d** Diagram of the mechanism by which trinucleotide repeat accumulation triggers a pathological loop leading to dysregulation of astrocyte differentiation. Data were analyzed using one-sample t-test (**a**, $n = 3$) or Kruskal–Wallis test followed by Dunn's multiple-comparison test (**b, c**). Statistical significance: *$p \leq 0.05$, **$p \leq 0.01$, ***$p \leq 0.001$.

production may remain phenotypically silent while predisposing astrocytes to actual dysfunction later in life.

Within this perspective, the reduced GFAP expression observed in HD astroglial progenitors may represent an early alteration masked by compensatory mechanisms in the dynamics of intermediate filaments and therefore not readily detectable in vivo. This scenario would be compounded by the fact that, while disease progresses, HD astrocytes undergo reactive transformation characterized by hypertrophy and increased expression of intermediate filament proteins, including GFAP [86, 87]. The elevated GFAP levels observed at late disease stages may, therefore, likely reflect a reactive "end-state" rather than a baseline HD GFAP-deficient phenotype, which may further obscure this early deficit.

Taken together, our findings point to a model in which early developmental perturbations in astroglial lineage specification may establish a latent vulnerability that unfolds progressively throughout the course of HD, likely contributing to the astrocytic pathology characteristic of the disease.

Within this framework, the identification of a druggable molecular circuitry underlying defective astrogliogenesis acquires particular relevance. Our data demonstrate that the EZH2–let-7g–LIN28 axis, which is dysregulated in HD neural progenitors, can be effectively targeted pharmacologically, leading to normalization of neural precursor proliferation and restoration of GFAP expression in astroglial progeny [14, 83, 84]. Notably, these interventions also ameliorated motor dysfunction in a Drosophila melanogaster model of HD, supporting the functional relevance of this pathway in vivo. Furthermore, we identified four distinct compounds that, despite functioning as canonical epigenetic drugs or modulators, operate through at least three different mechanisms of action. Each molecule targets one of the three key nodes in this molecular circuit, thereby counteracting the effects of mHTT and restoring astroglial support.

These findings point to a prospective therapeutic paradigm that may extend across multiple stages of disease progression. Early intervention—potentially during fetal or early postnatal development—could prevent defects in astroglial lineage specification. Yet, the same molecular targets would remain accessible in the adult brain, where astrocytes undergo reactive remodeling and faulty GFAP production in response to ongoing neurodegeneration, thereby enabling further therapeutic intervention at later disease stages.

We are now extending these findings to human HD brain organoids, where these compounds are being evaluated for efficacy and safety, with the aim of translating this approach into disease-modifying strategies targeting astrocyte dysfunction across different pathogenetic stages in HD.

MATERIAL AND METHODS

Knock-in zQ175 animal models

The zQ175 knock-in allele was derived from a spontaneous expansion of the CAG copy number in CAG-140 knock-in mice obtained from Jackson Laboratory (B6J.129S1-Htttm1Mfc/190JChdi). A fragment extending from 18 bp upstream of Htt exon 1 to 100 bp into intron 1 was replaced with human HTT sequence containing 140 repeats of a pure CAG tract [(CAG) nCAACAG], encoding polyglutamine. A floxed neomycin cassette was retained 1.3 kbp upstream of exon 1. While backcrossing onto C57BL/6 J, germline expansions of the CAG tract led to the identification of a mouse with 175 CAG repeats. This mouse was selectively bred to create a new subline, named zQ175. This line is identical in construct to CAG 140 knock-in mice, except for the CAG tract size. In these mutant mice, the CAG repeat number is subject to germline and somatic instability and may expand or contract. Homozygous and heterozygous mice are viable and fertile, with some characteristics resembling HD.

For our experiments, matings were set up with a male WT and a female positive for Htt zQ175, while zQ175 positive males were prevented from mating to avoid Htt meiotic instability. Mice were molecularly genotyped through PCR using DNA extracted from an ear biopsy.

All mice were housed in controlled conditions of temperature, which was maintained constant at 20–22 °C, and 12-h light-dark cycles, in individually ventilated cages (IVC – Techniplast GreenLine) and pathogen-free (SPF), according to the FELASA 2014 Guidelines. Animals sacrificed were euthanized with CO2 infusion and cervical dislocation, according to the D. Lgs. 26, 2014. All experiments were in accordance with the guidelines of the University of Trento and the Italian Ministry of Health (nr.781/2016-PR).

Isolation of neural stem cells from the mouse brain SVZ

Two wild-type (WT) control mice and three Q175 mice (male and female) were sacrificed through cervical dislocation for euthanasia. The heads were severed just above the cervical spinal cord using large scissors, and the brains were carefully extracted from the cranial base, placing them in a sterile 100 mm petri dish with sterile 1X PBS. Under a microscope, the forebrain SVZ region was dissected using a scalpel, making a coronal cut starting from the olfactory bulbs. Fine curved micro scissors were used to cut around the lateral ventricle, isolating it from the surrounding brain tissue. The dissected SVZ tissue was treated according to Gritti et al. [38]. Briefly, it was placed in a fresh petri dish containing a Papain solution and incubated in a CO2 incubator for 45 min. After the enzymatic digestion, the tissue was pelleted by centrifugation at 192 g for 10 min. The supernatant was removed, and approximately 200 microliters of neural stem cell medium was added. The tissue was triturated using a P200 micropipette. Following a second centrifugation at 192 g for 10 min, the supernatant was discarded, and the cell pellet was resuspended in 200 microliters of neural stem cell medium. The cells were then seeded in a T25 cell culture flask at a density of 10^4 cells/cm^2.

hiNSCs transplantation in nude mice

To evaluate the differentiation abilities of HD-hiNSCs and CTR-hiNSCs, in vivo, immunodeficient (Hsd: Athymic Nude-Foxn1nu) female mice, > 6 weeks old, provided by Envigo, were transplanted intra-striatum (antero-posterior: 0 mm; lateral: −2,5 mm; ventral: −2,7 mm), with ~300,000 hiNSCs/3 µL/mouse ($n = 3$ animals/cell line), authorization number 751/2019-PR. Transplanted animals were euthanized by overdose of anesthesia and perfused with a solution of 4% PFA in PBS-1X at 15 days after transplant. Brains were removed from the skull and post-fixed in a 4% PFA solution overnight. All the samples were cryoprotected by using a sucrose gradient (10, 20, and 30%), embedded in OCT (Optimal Cutting Temperature) matrix compound (Killik, Bio Optica, #05-9801), and frozen with nitrogen vapors. Brain sections were incubated with the following primary antibodies: huN, conjugated Alexa 488 - clone 235-1 (mouse, Millipore, #MAB1281A4, dilution: 1:200); hGFAP, clone SMI21 (mouse, BioLegend, #837202, dilution 1:600).

For the detection of primary antibodies, Alexa Fluor 488 and/or 594 labelled goat anti-mouse (488: Jackson, #115-545-205; 594: Invitrogen, #A21125) and/or goat anti-rabbit (488: Jackson, #111-545-144; 594: Invitrogen, #A11012) secondary antibodies, all diluted 1:1000, were used. Nuclei were labelled with DAPI.

Immunohistochemistry, tissue processing, and antibodies for zQ175 mice characterization

Brains from p7 zQ175-mice and controls (males and females) were sampled and post-fixed with PFA overnight, then cryoprotected as above. Immunohistochemical analyses were performed on three different litters (two originating from two different female mice with the disease, while one derived from a male HD mouse).

20 µm thick brain cryopreserved coronal sections were cut on a cryostat and collected in parallel series. Sections were incubated with the following primary antibodies: Ki-67 (rabbit, Novus Biologicals, #NB600-1252, dilution: 1:500); Ki-67 (mouse, Novus Biologicals, #NBP2-22112, dilution: 1:200); MASH1 (mouse, BD Pharmingen, #556604, dilution: 1:300); GFAP (mouse, Millipore, #MAB3402, dilution: 1:300); DCX (rabbit, Cell Signaling, #4604S, dilution: 1:400). For the detection of primary antibodies, Alexa Fluor 488 and/or 594 labelled goat anti-mouse (488: Jackson, #115-545-205; 594: Invitrogen, #A21125) and/or goat anti-rabbit (488: Jackson, #111-545-144; 594: Invitrogen, #A11012) secondary antibodies, all diluted 1:1000, were used. Nuclei were labelled with DAPI.

Immunohistochemical quantifications

The quantification analyses of the SVZ and RMS of Q175 and WT animals have been performed by measuring 2 to 4 serial coronal sections (20 µm thick, 7-8 animal/group) of the brain region spanning from the conjunction of the corpus callosum up to the emergence of the 3rd ventricle (circa 600 µm total). For each ventricle, adjacent 20X confocal images covering the RMS and the ventricular wall lining the striatum have been acquired. The quantification of Ki67+ and MASH1+ cells has been performed by a blinded observer, and, for each animal, the mean value of 2-4 ventricles was generated and plotted for statistical evaluation.

For the quantification of GFAP and DCX immunoreactive area, in each image, the ROI has been selected by encircling the SVZ and RMS (red area in the schematic as in Fig. 1a) based on DAPI stain, and default settings for thresholding have been applied to obtain the % of the immunoreactive area (%Area). For each animal, the mean % Area value of 2–4 ventricles was generated and plotted for the statistical evaluation. The % Area for each ventricle is the result of the following calculation: (sum of thresholded ROI)/(sum of unthresholded ROI) * 100. Results are shown as means ± SD. Confocal images were taken using the NIKON A1R microscope. For fluorescence quantification, the images have been acquired with the same settings across experimental groups. For quantitative image analysis, slides were coded prior to assessment, and investigators performing the measurements were blinded to genotype and experimental group allocation until completion of the analysis.

Human iPSC-derived neural stem cells production (hiNSCs)

Patient-derived iPSCs were generated at Fondazione IRCCS Casa Sollievo della Sofferenza under Ethics Committee-approved protocols (approval no. 136/CE). Written informed consent was obtained from all donors prior to sample collection. HD-iPSCs [43–45] were manually detached and plated in floating conditions. Nutristem-XF medium was gradually switched to KOSR medium (DMEM F-12, 20% Knock-out serum replacement (Gibco), 0.1 mM β-mercaptoethanol, 1X NEAA, 50U/ml Penicillin-Streptomycin, 2mM L-glutamine) where cells were maintained for 52 days. Neural precursor cells were selected using serum-free neurosphere growth medium, and after 10 days, cells were mechanically dissociated into single cells and replated at high density in the same medium. In this phase, a single cell produces a sphere that can be routinely split every 10–15 days: up to 20–30 times [47]. Cell line identity was verified by short tandem repeat (STR) profiling at the start of the project. Cells were routinely monitored for mycoplasma contamination.

Proliferation curves and % of cell death of mNSCs and hiNSCs

On day 0, neurospheres were mechanically split into single cells, 300.000 cells were seeded in serum-free neurosphere growth medium at 37 °C, 5% O2, and 5% CO2 for a week. Proliferation curves were determined using Trypan Blue dye (Sigma-Aldrich) by direct counting of stained and unstained cells after 7, 14, and 21 days of culture. The mean cell count/flask was recorded for each cell line, and cell numbers were plotted against culture time. Growth rates of cells were calculated by dividing the counted

cells by the seeding value (300.000 cells). % of dead cells was estimated by dividing the trypan-blue positive by the total number of cells and multiplying the obtained result by 100 to express it as a percentage. All experiments were performed at least in triplicate, unless otherwise indicated.

Quantitative real-time PCR (qRT-PCR)

Total RNAs were extracted using TRIzol reagent (Life Technologies). cDNAs were synthesized using the High-Capacity cDNA Reverse Transcription Kit (Applied Biosystems). For miRNA analyses, we used the TaqMan™ MicroRNA Reverse Transcription Kit (Applied Biosystems), according to the manufacturer's instructions. Real-Time PCR analyses were carried out using a 7900HT Fast Real-Time PCR system (Applied Biosystems). SYBR green reactions were performed using Power SYBR Green PCR Master Mix (Applied Biosystem) with the following PCR program: denaturation 95 °C for 10 min; amplification 95 °C for 10 s, 60 °C for 10 s, 72 °C for 30 s, all of which was repeated for 50 cycles; final elongation 72 °C for 7 min; final dissociation step 95 °C for 15 s, 60 °C for 15 s and 95 °C for 15 s. For each gene of interest, the protocol was as follows: each cDNA sample was tested in duplicate in a minimum of two independent biological experiments. The expression ratio of the target genes was calculated by using the $2^{-\Delta\Delta Ct}$ method, considering TBP as the reference gene, unless otherwise indicated.

Sybr Green Primers used for qPCR	Forward 5′-3′	Reverse 5′-3′
Ki-67 human	GAA AGA GTG GCA ACC TGC CTT C	GCA CCA AGT TTT ACT ACA TCT GCC
gfap human	GCG GGA TGG AGA GGG TAC TA	ATG TGG TGT CTT GTG GCT CA
ezh2 human	ACT GTA CTC GTT GTC CAA ACA	GTA TCC ACA TCC TCA GCG GG
lin28 human	CAC AAT GGG TGG GGG CTA TT	CCC AGA ACC TCT ACT TGC AT
Tbp human	CCG AAA CGC CGA ATA TAA TCC	AAA TCA GTG CCG TGG TTC GT
gapdh human	GTC TTC ACC ACC ATG GAG	CCA CCC TGT TGC TGT AGC
mcherry	CCC TCA GTT CAT GTA CGG CT	GCC GTC CTC GAA GTT CAT CA
lin28 mouse	CAG GCT TGG TAG CCA CTG AC	CAC GGA TGG ATT CCA GAC CC
Ezh2 mouse	TGT GGG CAT CGA ACG AGA AA	AGC AAG CTG GAA AAA CAA AGC A
tbp mouse	GCA CAG GAG CCA AGA GTG A	CCC ACC ATG TTC TGG ATC TT

Taqman Primers used for qPCR	Probe
pri-let7 human	Hs03303029_pri
let7 human	TM: 002282
mir16 human	Hs03303046
pri-let7 mouse	Mm03306155_pri
let7 mouse	Mm03306 155
mir16 mouse	Mm03306 169

To quantify differences in E(z) and lin28 gene expression between HD (*elav-Gal4 > 128QHtt*) and control (*elav-Gal4 > 16QHtt*) flies, RNA samples from adult heads were isolated using QIAzol reagent (Qiagen), according to the manufacturer's instructions. 2 µg of total RNA was reverse transcribed using oligo dT and SuperScript Reverse Transcriptase III (Invitrogen) according to the manufacturer's protocol. The qPCR reactions were carried out with PowerUp SYBR Green Master Mix for qPCR (Applied Biosystems) according to the manufacturer's protocol. Relative abundance of the different transcripts was determined using the $2^{-\Delta\Delta Ct}$ method [91] with the rp49 transcript as the reference gene. qRT-PCR experiments were performed in three independent biological replicates, each with three technical replicates. The qRT-PCR primer sequences are the following:

Sybr Green Primers used for qPCR	Forward 5′-3′	Reverse 5′-3′
E(Z)	AGT GGA AGA GGC GTG TCA AG	TGT GCT CGT CCC AGT TTC TTA T
lin28	ACT TCA TCA GCG AAT CCG GCA A	TCC CTT GGC CAC GTT GAA CC
rp49	GCG CAC CAA GCA CTT CAT C	TTG GGC TTG CGC CAT T

Clonal efficiency of mNSCs and hiNSCs

hiNSCs and mNSCs were resuspended in a growth medium for neurospheres. After scalar dilutions, we seeded them in a 24-well dish (Falcon®), previously pre-treated with Poly-L-lysine 0.01% (Sigma-Aldrich), at two different concentrations: 1000 cells/cm2 and 500 cells/cm2 per well. On day 7, we acquired optical microscope images with a 10X magnification, and we counted the number of neurospheres obtained per well. % of clonal efficiency was calculated following the formula below:

Each dot represents an independent experiment expressed as the mean analysis of microscopy images ($n = 3$ for mNSCs, $n = 20$ for CTR-hiNSCs, and $n = 11$ for HD-hiNSCs).

Differentiation of mNSCs and hiNSCs

The neurospheres were mechanically dissociated into single cells, then transferred for three days onto cultrex-coated glass coverslips at the density of 20.000 cells/coverslip without EGF and finally put into a mitogen-free medium (+2%FBS) to allow a spontaneous in vitro differentiation into neurons, astrocytes, and oligodendrocytes [47]. Differentiated cells were cultured for up to 17 days to obtain a mixture of neural cells containing astrocytes, neurons, and oligodendrocytes.

Immunofluorescence analyses of differentiated cells

Immunofluorescence analyses were performed at 10 and 17 days after bFGF/ EGF removal. Cells were fixed in freshly buffered 4% paraformaldehyde for 10 min at room temperature and permeabilized with 0.1% Triton X-100 for 10 min (except for GALC staining). After blocking with 10% normal goat serum (NGS), the cultures (mouse and human) were incubated overnight at 4 °C with the following antibodies: anti-TUBB3 (1:400 - BioLegend, # 801202); GFAP (1:200 - Dako, # Z033401-2); and GALC (1:200 - Sigma-Aldrich, #MAB342). Cells were incubated with the following secondary antibodies: anti-rabbit Alexa Fluor 488 and anti-mouse Alexa Fluor 555 (Invitrogen, # A11008 and # A21422), 1:1000. Nuclei staining was performed with Hoechst 33342 (Invitrogen). Microphotographs were taken using a Nikon C2 fluorescence microscope and NIS Elements 1.49 software and analyzed with ImageJ software. % of labeled cells/total nuclei, neurite length (m), and GFAP corrected total cell fluorescence (CTCF) are reported as means ± SD. Each dot represents the analysis of a confocal microscopy image, and all experiments were performed at least in triplicate.

Western blot analyses

Whole cell protein extracts were prepared using an appropriate volume of RIPA buffer 1X (Sigma-Aldrich) supplemented with Phosphatase Inhibitors and Protease Inhibitors cocktails (Sigma-Aldrich). Protein quantification was performed through the BCA Assay (Bio-rad) using Varioskan LUX (ThermoFisher Scientific). Lysates were loaded into Mini-Protean TGX gels 4–15% (Bio-rad) and transferred to a nitrocellulose membrane using Trans-blot Turbo (Bio-rad). Membranes were washed for 5 min in Tris Buffer Saline (TBS) supplemented with 1% Tween-20 (Thermo Fisher Scientific) and then blocked with 5% non-fat milk in 1X TBS-Tween for 1 h at room temperature. Primary antibodies (anti-GAPDH: 1:1000—Sigma-Aldrich, # G9545; anti-GFAP 1:1000-Dako, # Z033401-2; anti-EZH2 1:1000-Cell

Signaling Technology, # 5246; anti-LIN28 1:1000-Abcam, #ab46020; anti-mCherry 1:1000-Abcam, #ab167453; anti-ACTIN 1:1000-Sigma-Aldrich, # MAB1501) were diluted in a blocking solution and incubated at 4°C overnight. Membranes were washed three times with 1X TBS-Tween for 10 min; then secondary antibodies (Anti-mouse 1:3000—Bio-rad, Anti-rabbit 1:5000—Bio-rad) were incubated for 1 h at room temperature. After three washing steps, the proteins were revealed with ECL Crescendo (Merck Millipore) according to the manufacturer's instructions. Images were acquired using the iBright (ThermoFisher), and image processing and densitometric quantification were performed using ImageJ software.

Original blots are present in the supplementary material.

Histone methyltransferase activity/inhibition measurement

Nuclear extracts were prepared using the EpiQuik Nuclear Extraction Kit I (EpingenTek) and added to the EpiQuik Histone Methyltransferase Activity/Inhibition Assay Kit (H3-K27, EpingenTek) following the manufacturer's instructions. Absorbances were measured using Varioskan LUX reader (ThermoFisher), and HMT activity was calculated using the formula

$$\mathrm{OD(sample\text{-}blank)}$$

$$\mathrm{Activity(ng/h/mg)} =\!\!\rightarrow \mathrm{x1000}$$

$$\mathrm{Protein\ amount}(\mu g)\mathrm{x\ hour\ x\ slope}$$

Glutamate assay

Cells (CTR-hiNSCs and HD-hiNSCs) were plated in 24-well plates (25000 cells/well). The culture medium was collected from CTR-hiNSCs and HD-hiNSCs and centrifuged at 10,000 $g \times 15'$ to remove insoluble debris. Glutamate concentration was measured by a colorimetric assay, according to the manufacturer's instructions (MAK004 Sigma-Aldrich). Protein extract from RIPA buffer lysis was quantified by BCA assay and used for normalization.

Viral infection protocol

Vectors pCAG 17Q HTT-N548 and pCAG 73Q HTT-548 were obtained as described in Migazzi et al. 2021 [51]. On day 0, neurospheres were mechanically disrupted, and 500.000 cells were seeded in 2 different flasks, each one infected by transduction at a multiplicity of infection (MOI) of 10 with 17Q and 73Q vectors, respectively. After 24 h the medium was replaced by fresh virus-free neurospheres medium, and 7 days after infection, cell pellets were collected for subsequent analyses.

Transcriptomic analysis

GeneChip Human Transcriptome Array (HTA) 2.0 (Affymetrix) was used for the quantification of transcript levels. All procedures were conducted according to the manufacturer's protocols (Affymetrix Inc., Santa Clara, CA, USA). Briefly, for each array, complementary RNA (cRNA) was prepared from 200 ng of total RNA according to the Affymetrix Whole Transcript (WT) protocol. The cRNA was used to generate single-stranded DNA, which was fragmented and biotinylated. The labeled single-stranded DNA was hybridized on Affymetrix HTA 2.0 microarrays. The microarrays were then washed and stained with a streptavidin-phycoerythrin conjugate in an Affymetrix Fluidics Station 450. The microarrays were scanned with a GeneChip Scanner 3000 7 G (Affymetrix). All GeneChips were visually inspected for irregularities. The global method of scaling (or normalization) was applied to all GeneChips. The percentage of present genes and the ratio of endogenous genes indicated a high overall quality of samples and assays. Oligo (v. 1.62.1) package from Bioconductor was used to extract quality measurements from the raw CEL files and perform the RMA normalization [94], and the affycore tools (v. 1.70) package was used for annotation. 3525 less variable probsets among the samples (~5%) were removed by using the genefilter (v. 1.80.2) package from Bioconductor (variance cut off=0.05). Differential gene expression analysis was performed on protein-coding genes using the limma package (v. 3.54.0) [95]. Differentially expressed genes were considered significant if their p value after Bonferroni correction was < 0.05. Gene Ontology Biological Processes (GO-BP) (v.2021) and Reactome (v.2022) enrichment analyses for down-regulated ($n = 383$) and up-regulated ($n = 488$) coding genes in HD-hiNSC relative to CTR-hiNSC were evaluated using Fisher's Exact test, using the enrichR R package [96]. GO and Reactome terms were considered significantly enriched if their p value after Bonferroni correction was < 0.001. Enrichment analyses between the established markers identified by Su [49] (10 major cell clusters and 9 astrocyte subpopulations) and up- and down-regulated coding genes in HD-hiNSC relative to CTR-hiNSC were evaluated using Fisher's Exact test, where the background set consisted of all expressed coding genes ($n = 17677$). Cell classes were considered significantly enriched if their p value after Bonferroni correction was < 0.001.

ChIP-PCR

Chromatin immunoprecipitation (ChIP) was performed as previously described [97]. Epigenetic Restoration of Fetal-like IGF1 Signaling Inhibits Leukemia Stem Cell Activity with validated antibodies against H3K27me3 (Cat. C15410069-50, Diagenode), Ezh2 (Cat.49-1043, Thermofisher), and rabbit IgG (Cat. 2729, Cell Signaling Technology). Briefly, cells were treated with 1% formaldehyde for 10 min at 37 °C, lysed in 1% SDS, 10 mM EDTA, and 50 mM Tris (pH 8.1), and sonicated to obtain DNA fragments ranging in length from 200 bp to 600 bp. Subsequently, the chromatin was immunoprecipitated with antibodies. After overnight incubation with antisera at 4 °C, we captured immunoprecipitated chromatin with Protein A agarose beads, which we subsequently washed, and eluted the bound chromatin. After reversal of crosslinks, we purified DNA using the QIAquick PCR purification kit (Qiagen). ChIP DNA was quantified using a Qubit dsDNA HS Assay Kit (Cat. Q32851, ThermoFisher Scientific) and the quality was assessed by the 4200 TapeStation System using High Sensitivity D1000 Reagents (Cat. 5067-5585, Agilent Technologies). DNA enrichment was assessed using the QX200 ddPCR EvaGreen Supermix (Bio-Rad, #1864033) on the QX200 Droplet Digital PCR system (Bio-Rad). The ddPCR data were analyzed with QuantaSoft Software. Statistical analyses were performed using GraphPad Prism (version 10.4.2). A p-value < 0.05 was considered statistically significant. The primer sequences used for amplification are listed in Table S1.

AmpliconForward primerReverse Primer

GFAP 0.0 5′-GTCTCCTCTCCATCCTGCTCT-3′ 5′-CTATGCCAGGGGGTGTTG-3′

GFAP -4.6 5′-GACCAGCAAGTCTGTTCATC-3′ 5′-TTTCTCCCTGCCTCTAAACT-3′

ZNF333 5′-AGCCTTCAATCAGCCATCATCCCT-3′ 5′-TCTGGTATGGGTTCGC AGATGTGT3′

GAPDH 5′-TACTAGCGGTTTTACGGGCG-3′ 5′-TCGAACAGGAGGAGCAGA-GAGCGA-3′

ChIP-sequencing analysis

The ChIP-Seq data were reanalyzed from GEO accession GSM2879087 [98], aligned against the human genome hg19, and visualized using the Integrative Genomics Viewer (IGV). Peaks were called with Model-based Analysis for ChIP-seq (MACS2) using default parameters after normalization with input as a control. The peaks with p-value < 0.05 were retained.

Pharmacological cell treatments

Cells were treated with EZH2 inhibitors (TAZ 1 µM, MS1943 100 nM) and Let-7g-restoring compounds (IPA3 10 nM, 1632 0.6 µM), selected via functional and viability assays. Treatments began at the onset of spontaneous differentiation (growth factor withdrawal) and were refreshed every three days throughout the experiment.

Fly stocks and treatments

All transgenic fly stocks used in this study were obtained from the Bloomington Drosophila stock center http://flystocks.bio.indiana.edu and are listed below:

UAS-HTT.128Q (w)^{1118} ; P{w[+mC]=UAS-HTT.128Q.FL}f27b, #33808;

UAS-HTT.16Q (w)^{1118} ; P{w[+mC]=UAS-HTT.16Q.FL}F24/CyO, #33810;

elav-Gal4 (P{*GawB*}*elav*^{C155}, #458).

A detailed description of all the lines is given at FlyBase http://flybase.org. Flies were raised at 25 °C on a standard cornmeal-sucrose-yeast-agar medium.

Drosophila larvae or adult flies were grown on standard medium supplemented with each of the epigenetic inhibitors at the following final concentrations: Tazemetostat 50 µM, MS1943 20 µM, IPA3 10 µM, 1632 50 µM. Control groups, grown on standard medium containing only the solvent (DMSO), were included alongside each experimental group. All the experiments were performed at 29 °C.

Climbing assay

The negative geotaxis assay was performed as previously described [99]. For each treatment, groups of 10 flies, male and female flies 6–7 days old, were anesthetized with CO2, allowed to recover for 2 h, and then

transferred into empty glass tubes (9.5 cm × 2.5 cm). In each assay, groups of 10 flies were tapped down and evaluated for their ability to cross an 8 cm line within 10 s, with a total of 10 trials per assay. At least 150 flies were tested for each experimental group. Data are presented as mean ± SEM and analyzed using one-way ANOVA, followed by Dunnett's post hoc test for comparisons. All statistical analyses were performed using GraphPad Prism, with a significance threshold set at $p \leq 0.05$.

Statistical analyses

All experiments were performed with at least three independent biological replicates. In the scatter plots, each data point represents one independent biological replicate (n). Statistical analyses were conducted using GraphPad Prism 8. For small sample sizes ($n < 8$), data were assumed to be normally distributed; for larger samples ($8 < n < 20$), normality was tested. Data were analyzed using unpaired two-tailed Welch's t-tests or one-way/two-way ANOVA followed by Bonferroni's post hoc correction. Data sets with more than 20 samples were analyzed using non-parametric tests, specifically the two-tailed Mann–Whitney or Kruskal–Wallis tests, followed by Dunn's for multiple comparisons. Statistical significance was defined as $^{*}p \leq 0.05$, $^{**}p \leq 0.01$, and $^{***}p \leq 0.001$. Both transcriptomic and ChIP analyses were performed as indicated in the relevant sections. For in vitro experiments, the sample size was determined based on previous studies employing similar experimental approaches. For animal experiments, sample sizes were determined by the availability of animals from independent litters. Whenever possible, animals from multiple litters were included to reduce litter-specific effects. Randomization was not performed in this study, as animals were classified into diseased and healthy groups based on their genetic condition.

DATA AVAILABILITY

All data supporting the findings of this study are available within the article and its supplementary information files. Any data or materials that can be shared are released via a Material Transfer Agreement. Original uncropped western blots are provided in the supplementary materials. All other raw data are available from the corresponding author upon reasonable request.

REFERENCES

1. Hinton Sean C, Paulsen Jane S, Hoffmann Raymond G, Reynolds Norman C, Zimbelman Janice L, Rao Stephen M. Motor timing variability increases in preclinical Huntington's disease patients as the estimated onset of motor symptoms approaches. J Int Neuropsychol Soc. 2007;13:539–543.
2. Duff K, Paulsen JS, Beglinger LJ, Langbehn DR, Stout JC. Predict-HD Investigators of the Huntington Study Group. Psychiatric symptoms in Huntington's disease before diagnosis: the Predict-HD study. Biol Psychiatry. 2007;62:1341–1346.
3. Solomon AC, Stout JC, Johnson SA, Langbehn DR, Aylward EH, Brandt J, et al. Verbal episodic memory declines prior to diagnosis in Huntington's disease. Neuropsychologia. 2007;45:1767–1776.
4. Lee JM, Ramos EM, Lee JH, Gillis T, Mysore JS, Hayden MR, et al. CAG repeat expansion in Huntington disease determines age at onset in a fully dominant fashion. Neurology. 2012;78:690–695.
5. Nopoulos P, Magnotta VA, Mikos A, Paulson H, Andreasen NC, Paulsen JS. Morphology of the cerebral cortex in preclinical Huntington's disease. Am J Psychiatry. 2007;164:1428–1434.
6. Paulsen JS, Ready RE, Hamilton JM, Mega MS, Cummings JL. Neuropsychiatric aspects of Huntington's disease. J Neurol Neurosurg Psychiatry. 2001;71:310–314.
7. Barquero-Jiménez MS, Gómez-Tortosa E. [Cognitive disorders in patients with Huntington's disease]. Rev Neurol. 2001;32:1067–1071.
8. van der Plas E, Langbehn DR, Conrad AL, Koscik TR, Tereshchenko A, Epping EA, et al. Abnormal brain development in child and adolescent carriers of mutant huntingtin. Neurology. 2019;93:e1021–e1030.
9. Schultz JL, Epping EA, van der Plas E, Magnotta VA, Nopoulos PC. Striatal development in early-onset Huntington's disease. Mov Disord. 2022;37:2459–2460.
10. Estevez-Fraga C, Altmann A, Parker CS, Scahill RI, Costa B, Chen Z, et al. Genetic topography and cortical cell loss in Huntington's disease link development and neurodegeneration. Brain. 2023;146:4532–4546.
11. Stoker TB, Mason SL, Greenland JC, Holden ST, Santini H, Barker RA. Huntington's disease: diagnosis and management. Pr Neurol. 2022;22:32–41.
12. Dionisio LE, Yang XW. Group dynamics goes awry: PolyQ-expanded huntingtin gains unwanted partners. Cell Syst. 2022;13:268–270.
13. Xu H, Bensalel J, Raju S, Capobianco E, Lu ML, Wei J. Characterization of huntingtin interactomes and their dynamic responses in living cells by proximity proteomics. J Neurochem. 2023;164:512–528.
14. Liu CF, Younes L, Tong XJ, Hinkle JT, Wang M, Phatak S, et al. Longitudinal imaging highlights preferential basal ganglia circuit atrophy in Huntington's disease. Brain Commun. 2023;5:fcad214.
15. Mätlik K, Baffuto M, Kus L, Davis DA, Paul MR, Carroll TS, et al. Cell type-specific CAG repeat expansions and toxicity of mutant huntingtin in human striatum and cerebellum. Nat Genet. 2024;56:383–394.
16. Vonsattel JPG, Keller C, Cortes Ramirez EP. Huntington's disease - neuropathology. Handb Clin Neurol. 2011;100:83–100.
17. Singh S, Singh TG. Role of nuclear factor kappa B (NF-κB) signalling in neurodegenerative diseases: a mechanistic approach. Curr Neuropharmacol. 2020;18:918–935.
18. Mor A, Tankiewicz-Kwedlo A, Krupa A, Pawlak D. Role of the kynurenine pathway in oxidative stress during neurodegenerative disorders. Cells. 2021;10:1603.
19. Palpagama TH, Waldvogel HJ, Faull RLM, Kwakowsky A. The role of microglia and astrocytes in Huntington's disease. Front Mol Neurosci. 2019;12:258.
20. Wilton DK, Stevens B. The contribution of glial cells to Huntington's disease pathogenesis. Neurobiol Dis. 2020;143:104963.
21. Henningsen JB, Soylu-Kucharz R, Björkqvist M, Petersén Å. Effects of excitotoxicity in the hypothalamus in transgenic mouse models of Huntington disease. Heliyon. 2021;7:e07808.
22. Estrada-Sánchez AM, Rebec GV. Corticostriatal dysfunction and glutamate transporter 1 (GLT1) in Huntington's disease: interactions between neurons and astrocytes. Basal Ganglia. 2012;2:57–66.
23. Paulsen JS, Magnotta VA, Mikos AE, Paulson HL, Penziner E, Andreasen NC, et al. Brain structure in preclinical Huntington's disease. Biol Psychiatry. 2006;59:57–63.
24. Hickman RA, Faust PL, Rosenblum MK, Marder K, Mehler MF, Vonsattel JP. Developmental malformations in Huntington disease: neuropathologic evidence of focal neuronal migration defects in a subset of adult brains. Acta Neuropathol. 2021;141:399–413.
25. Barnat M, Capizzi M, Aparicio E, Boluda S, Wennagel D, Kacher R, et al. Huntington's disease alters human neurodevelopment. Science. 2020;369:787–793.
26. Lim RG, Al-Dalahmah O, Wu J, Gold MP, Reidling JC, Tang G, et al. Huntington disease oligodendrocyte maturation deficits revealed by single-nucleus RNAseq are rescued by thiamine-biotin supplementation. Nat Commun. 2022;13:7791.
27. Kohl Z, Regensburger M, Aigner R, Kandasamy M, Winner B, Aigner L, et al. Impaired adult olfactory bulb neurogenesis in the R6/2 mouse model of Huntington's disease. BMC Neurosci. 2010;11:114.
28. Phillips W, Morton AJ, Barker RA. Abnormalities of neurogenesis in the R6/2 mouse model of Huntington's disease are attributable to the in vivo microenvironment. J Neurosci. 2005;25:11564–11576.
29. Silva AC, Ferreira IL, Hayden MR, Ferreiro E, Rego AC. Characterization of subventricular zone-derived progenitor cells from the mild and late symptomatic YAC128 mouse model of Huntington's disease. Biochim Biophys Acta Mol Basis Dis. 2018;1864:34–44.
30. Curtis MA, Penney EB, Pearson AG, van Roon-Mom WM, Butterworth NJ, Dragunow M, et al. Increased cell proliferation and neurogenesis in the adult human Huntington's disease brain. Proc Natl Acad Sci USA. 2003;100:9023–9027.
31. Curtis MA, Low VF, Faull RLM. Neurogenesis and progenitor cells in the adult human brain: a comparison between hippocampal and subventricular progenitor proliferation. Dev Neurobiol. 2012;72:990–1005.
32. Curtis MA, Penney EB, Pearson J, Dragunow M, Connor B, Faull RL. The distribution of progenitor cells in the subependymal layer of the lateral ventricle in the normal and Huntington's disease human brain. Neuroscience. 2005;132:777–788.
33. McCollum MH, Leon RT, Rush DB, Guthrie KM, Wei J. Striatal oligodendrogliogenesis and neuroblast recruitment are increased in the R6/2 mouse model of Huntington's disease. Brain Res. 2013;1518:91–103.
34. Southwell AL, Smith-Dijak A, Kay C, Sepers M, Villanueva EB, Parsons MP, et al. An enhanced Q175 knock-in mouse model of Huntington disease with higher mutant huntingtin levels and accelerated disease phenotypes. Hum Mol Genet. 2016;25:3654–3675.
35. Menalled LB, Sison JD, Dragatsis I, Zeitlin S, Chesselet MF. Time course of early motor and neuropathological anomalies in a knock-in mouse model of Huntington's disease with 140 CAG repeats. J Comp Neurol. 2003;465:11–26.
36. Carty N, Berson N, Tillack K, Thiede C, Scholz D, Kottig K, et al. Characterization of HTT inclusion size, location, and timing in the zQ175 mouse model of Huntington's disease: an in vivo high-content imaging study. PLoS ONE. 2015;10:e0123527.
37. Galli R, Gritti A, Vescovi AL. Adult neural stem cells. Methods Mol Biol. 2008;438:67–84.
38. Gritti A, Parati EA, Cova L, Frolichsthal P, Galli R, Wanke E, et al. Multipotential stem cells from the adult mouse brain proliferate and self-renew in response to basic fibroblast growth factor. J Neurosci. 1996;16:1091–1100.
39. Osipovitch M, Asenjo Martinez A, Mariani JN, Cornwell A, Dhaliwal S, Zou L, et al. Human ESC-derived chimeric mouse models of Huntington's disease reveal cell-

intrinsic defects in glial progenitor cell differentiation. Cell Stem Cell. 2019;24:107–122.e7.
40. Huang B, Wei W, Wang G, Gaertig MA, Feng Y, Wang W, et al. Mutant Huntingtin downregulates myelin regulatory factor-mediated myelin gene expression and affects mature oligodendrocytes. Neuron. 2015;85:1212–1226.
41. Khakh BS, Goldman SA. Astrocytic contributions to Huntington's disease pathophysiology. Ann NY Acad Sci. 2023;1522:42–59.
42. Ferrari Bardile C, Garcia-Miralles M, Caron NS, Rayan NA, Langley SR, Harmston N, et al. Intrinsic mutant HTT-mediated defects in oligodendroglia cause myelination deficits and behavioral abnormalities in Huntington disease. Proc Natl Acad Sci USA. 2019;116:9622–9627.
43. Rosati J, Bidollari E, Rotundo G, Ferrari D, Torres B, Bernardini L, et al. Generation of induced pluripotent stem cell line, CSSi002-A (2851), from a patient with juvenile Huntington disease. Stem Cell Res. 2018;27:86–89.
44. Bidollari E, Rotundo G, Ferrari D, Candido O, Bernardini L, Consoli F, et al. Generation of induced pluripotent stem cell line, CSSi004-A (2962), from a patient diagnosed with Huntington's disease at the presymptomatic stage. Stem Cell Res. 2018;28:145–148.
45. Rotundo G, Bidollari E, Ferrari D, Spasari I, Bernardini L, Consoli F, et al. Generation of the induced pluripotent stem cell line CSSi006-A (3681) from a patient affected by advanced-stage Juvenile-Onset Huntington's disease. Stem Cell Res. 2018;29:174–178.
46. Isaja L, Ferriol-Laffouillere SL, Mucci S, Rodríguez-Varela MS, Romorini L. Embryoid bodies-based multilineage differentiation of human embryonic stem cells grown on feeder-free conditions. Methods Mol Biol. 2022;2520:189–198.
47. Rosati J, Ferrari D, Altieri F, Tardivo S, Ricciolini C, Fusilli C, et al. Establishment of stable iPS-derived human neural stem cell lines suitable for cell therapies. Cell Death Dis. 2018;9:937.
48. Miyashita S, Hoshino M. Transit amplifying progenitors in the cerebellum: similarities to and differences from transit amplifying cells in other brain regions and between species. Cells 2022;11:726.
49. Su Y, Zhou Y, Bennett ML, Li S, Carceles-Cordon M, Lu L, et al. A single-cell transcriptome atlas of glial diversity in the human hippocampus across the postnatal lifespan. Cell Stem Cell. 2023;30:113.
50. Tripathy D, Vignoli B, Ramesh N, Polanco MJ, Coutelier M, Stephen CD, et al. Mutations in TGM6 induce the unfolded protein response in SCA35. Hum Mol Genet. 2017;26:3749–3762.
51. Migazzi A, Scaramuzzino C, Anderson EN, Tripathy D, Hernández IH, Grant RA, et al. Huntingtin-mediated axonal transport requires arginine methylation by PRMT6. Cell Rep. 2021;35:108980.
52. Seong IS, Woda JM, Song JJ, Lloret A, Abeyrathne PD, Woo CJ, et al. Huntingtin facilitates polycomb repressive complex 2. Hum Mol Genet. 2010;19:573–583.
53. Sparmann A, Xie Y, Verhoeven E, Vermeulen M, Lancini C, Gargiulo G, et al. The chromodomain helicase Chd4 is required for Polycomb-mediated inhibition of astroglial differentiation. EMBO J. 2013;32:1598–1612.
54. Barghout SH, Machado RAC, Barsyte-Lovejoy D. Chemical biology and pharmacology of histone lysine methylation inhibitors. Biochim Biophys Acta Gene Regul Mech. 2022;1865:194840.
55. Knutson SK, Warholic NM, Wigle TJ, Klaus CR, Allain CJ, Raimondi A, et al. Durable tumor regression in genetically altered malignant rhabdoid tumors by inhibition of methyltransferase EZH2. Proc Natl Acad Sci USA. 2013;110:7922–7927.
56. Qadeer ZA, Valle-Garcia D, Hasson D, Sun Z, Cook A, Nguyen C, et al. ATRX in-frame fusion neuroblastoma is sensitive to EZH2 inhibition via modulation of neuronal gene signatures. Cancer Cell. 2019;36:512–527.e9.
57. Januario T, Ye X, Bainer R, Alicke B, Smith T, Haley B, et al. PRC2-mediated repression of SMARCA2 predicts EZH2 inhibitor activity in SWI/SNF mutant tumors. Proc Natl Acad Sci USA. 2017;114:12249–12254.
58. Ma A, Stratikopoulos E, Park KS, Wei J, Martin TC, Yang X, et al. Discovery of a first-in-class EZH2 selective degrader. Nat Chem Biol. 2020;16:214–222.
59. Guajardo L, Aguilar R, Bustos FJ, Nardocci G, Gutiérrez RA, van Zundert B, et al. Downregulation of the polycomb-associated methyltransferase Ezh2 during maturation of hippocampal neurons is mediated by microRNAs Let-7 and miR-124. Int J Mol S. 2020;21:8472.
60. Chang HM, Triboulet R, Thornton JE, Gregory RI. A role for the Perlman syndrome exonuclease Dis3l2 in the Lin28-let-7 pathway. Nature. 2013;497:244–248.
61. Ustianenko D, Hrossova D, Potesil D, Chalupnikova K, Hrazdilova K, Pachernik J, et al. Mammalian DIS3L2 exoribonuclease targets the uridylated precursors of let-7 miRNAs. RNA. 2013;19:1632–1638.
62. Roos M, Pradère U, Ngondo RP, Behera A, Allegrini S, Civenni G, et al. A small-molecule inhibitor of Lin28. ACS Chem Biol. 2016;11:2773–2781.
63. Lin S, Gregory RI. Identification of small-molecule inhibitors of Zcchc11 TUTase activity. RNA Biol. 2015;12:792–800.
64. Romero E, Cha GH, Verstreken P, Ly CV, Hughes RE, Bellen HJ, et al. Suppression of neurodegeneration and increased neurotransmission caused by expanded full-length huntingtin accumulating in the cytoplasm. Neuron. 2008;57:27–40.
65. Robinow S, White K. The locus elav of Drosophila melanogaster is expressed in neurons at all developmental stages. Dev Biol. 1988;126:294–303.
66. Lewis EA, Smith GA. Using Drosophila models of Huntington's disease as a translatable tool. J Neurosci Methods. 2016;265:89–98.
67. Oh J, Catherine C, Kim ES, Min KW, Jeong HC, Kim H, et al. Engineering a membrane protein chaperone to ameliorate the proteotoxicity of mutant huntingtin. Nat Commun. 2025;16:737.
68. Chen ZhefanStephen, Peng ShaohongIsaac, Leong Lok I, Gall-Duncan Terence, Wong Nathan Siu Jun, Li Tsz Ho, et al. Mutant huntingtin induces neuronal apoptosis via derepressing the non-canonical poly(A) polymerase PAPD5. Nat Commun. 2025;16:3307.
69. Steffan JS, Agrawal N, Pallos J, Rockabrand E, Trotman LC, Slepko N, et al. SUMO modification of Huntingtin and Huntington's disease pathology. Science. 2004;304:100–104.
70. Lu XH, Mattis VB, Wang N, Al-Ramahi I, van den Berg N, Fratantoni SA, et al. Targeting ATM ameliorates mutant Huntingtin toxicity in cell and animal models of Huntington's disease. Sci Transl Med. 2014;6:268ra178.
71. Jung J, Bonini N. CREB-binding protein modulates repeat instability in a Drosophila model for polyQ disease. Science. 2007;315:1857–1859.
72. Krzystek Thomas J, Rathnayake Rasika, Zeng Jia, Huang Jing, Iacobucci Gary, Yu Michael C, et al. Opposing roles for GSK3β and ERK1-dependent phosphorylation of huntingtin during neuronal dysfunction and cell death in Huntington's disease. Cell Death Dis. 2025;16:328.
73. Muqit MM, Feany MB. Modelling neurodegenerative diseases in Drosophila: a fruitful approach? Nat Rev Neurosci. 2002;3:237–243.
74. Madabattula ST, Strautman JC, Bysice AM, O'Sullivan JA, Androschuk A, Rosenfelt C, et al. Quantitative analysis of climbing defects in a Drosophila model of neurodegenerative disorders. J Vis Exp 2015;e52741. https://doi.org/10.3791/52741.
75. Moss EG, Tang L. Conservation of the heterochronic regulator Lin-28, its developmental expression and microRNA complementary sites. Dev Biol. 2003;258:432–442.
76. Makeeva VS, Dyrkheeva NS, Lavrik OI, Zakian SM, Malakhova AA. Mutant-Huntingtin molecular pathways elucidate new targets for drug repurposing. Int J Mol Sci. 2023;24:16798.
77. Jurcau A. Molecular pathophysiological mechanisms in Huntington's disease. Biomedicines 2022;10:1432.
78. Ferrari Bardile C, Radulescu CI, Pouladi MA. Oligodendrocyte pathology in Huntington's disease: from mechanisms to therapeutics. Trends Mol Med. 2023;29:802–816.
79. Ferrari Bardile C, Sidik H, Quek R, Yusof NABM, Garcia-Miralles M, Pouladi MA. Abnormal spinal cord myelination due to oligodendrocyte dysfunction in a model of Huntington's disease. J Hunt Dis. 2021;10:377–384.
80. Casella C, Lipp I, Rosser A, Jones DK, Metzler-Baddeley C. A critical review of white matter changes in Huntington's disease. Mov Disord. 2020;35:1302–1311.
81. Al-Dalahmah O, Sosunov AA, Shaik A, Ofori K, Liu Y, Vonsattel JP, et al. Single-nucleus RNA-seq identifies Huntington disease astrocyte states. Acta Neuropathol Commun. 2020;8:19.
82. Juopperi TA, Kim WR, Chiang CH, Yu H, Margolis RL, Ross CA, et al. Astrocytes generated from patient-induced pluripotent stem cells recapitulate features of Huntington's disease patient cells. Mol Brain. 2012;5:17.
83. von Schimmelmann M, Feinberg PA, Sullivan JM, Ku SM, Badimon A, Duff MK, et al. Polycomb repressive complex 2 (PRC2) silences genes responsible for neurodegeneration. Nat Neurosci. 2016;19:1321–1330.
84. Hirabayashi K, Shiota K, Yagi S. DNA methylation profile dynamics of tissue-dependent and differentially methylated regions during mouse brain development. BMC Genomics. 2013;14:82.
85. Godin JD, Poizat G, Hickey MA, Maschat F, Humbert S. Mutant huntingtin-impaired degradation of beta-catenin causes neurotoxicity in Huntington's disease. EMBO J. 2010;29:2433–2445.
86. Shahim P, AlQahtani A, Kokkinis AD, Kazmi N, Ezuma-Ngwu M, Misra J, et al. CSF and blood neuronal injury biomarkers in spinal bulbar muscular atrophy and amyotrophic lateral sclerosis 4. Brain Commun. 2025;7:fcaf275.
87. Tian Q, Greig EE, Walker KA, Duggan MR, Yang Z, Moghekar A, et al. Longitudinal patterns of brain aging and neurodegeneration among older adults with dual decline in memory and gait. Alzheimers Dement. 2025;21:e14612.
88. Sood A, Preeti K, Fernandes V, Khatri DK, Singh SB. Glia: a major player in glutamate-GABA dysregulation-mediated neurodegeneration. J Neurosci Res. 2021;99:3148–3189.
89. Tan AYS, Tippett LJ, Turner CP, Swanson MEV, Park TIH, Curtis MA, et al. Microglial proliferation and astrocytic protein alterations in the human Huntington's disease cortex. Neurobiol Dis. 2024;198:106554.
90. Verkhratsky A, Hol EM, de Witte LD, Aronica E. General pathophysiology of neuroglia. Handb Clin Neurol. 2025;210:3–7.

91. Livak KJ, Schmittgen TD. Analysis of relative gene expression data using real-time quantitative PCR and the 2(-Delta Delta C(T)) Method. Methods. 2001;25:402–408.
92. Pekny M, Pekna M. Astrocyte intermediate filaments in CNS pathologies and regeneration. J Pathol. 2004;204:428–437.
93. Liedtke W, Edelmann W, Bieri PL, Chiu FC, Cowan NJ, Kucherlapati R, et al. GFAP is necessary for the integrity of CNS white matter architecture and long-term maintenance of myelination. Neuron. 1996;17:607–615.
94. Carvalho BS, Irizarry RA. A framework for oligonucleotide microarray preprocessing. Bioinformatics. 2010;26:2363–2367.
95. Smyth GK. Linear models and empirical Bayes methods for assessing differential expression in microarray experiments. Stat Appl Genet Mol Biol. 2004;3. https://doi.org/10.2202/1544-6115.1027.
96. Xie Z, Bailey A, Kuleshov MV, Clarke DJB, Evangelista JE, Jenkins SL, et al. Gene set knowledge discovery with Enrichr. Curr Protoc. 2021;1:e90.
97. Giambra V, Gusscott S, Gracias D, Song R, Lam SH, Panelli P, et al. Epigenetic restoration of fetal-like IGF1 signaling inhibits leukemia stem cell activity. Cell Stem Cell. 2018;23:714–726.e7.
98. Kim J, Lee Y, Lu X, Song B, Fong KW, Cao Q, et al. Polycomb- and methylation-independent roles of EZH2 as a transcription activator. Cell Rep. 2018;4:25.
99. Cappucci U, Proietti M, Casale AM, Schiavo S, Chiavarini S, Accardo S, et al. Assessing genotoxic effects of plastic leachates in Drosophila melanogaster. Chemosphere. 2024;361:142440.

AUTHOR CONTRIBUTIONS

JDR and ALV conceived the project, wrote the paper, and supervised experiments; AC, GRU, AMGG, GR, EMT, and AD performed cell curves, qRT-PCR, western blotting, and immunofluorescence analyses on mice and human neurospheres. IL, RMC, MG, and DF performed immunohistochemical analyses on the mice SVZ, AM, MP, and MBA produced by pCAG 17Q HTT-N548 and pCAG 73Q HTT-548 viruses. AV and EB produced mice neurospheres. OP performed transcriptomic experiments. V.G. and MC performed Chromatin-immunoprecipitation. AR and MC, SDA, and CB performed glutamate analyses. DR, SV, and AM contributed to drug design and optimization. AMC, UC, and LP performed Drosophila experiments. ADL performed CAG and STR analyses. GB and MB collected in vivo samples. DDA designed and conducted bioinformatics analyses and critically interpreted the results. FS analyzed the results. Funding was acquired by JDR, ALV, and AM. The project was supervised and administered by JDR and ALV. The original draft was written by JDR, MP, BR, and ALV. All authors participated in reviewing and editing the manuscript.

FUNDING

This work was supported by the Italian Ministry of Health, 5×1000 to JDR; a grant from Fondazione Prosolidar, 508-2021_IT to ALV and JDR; PRIN2022, P2022FESRR to A.M., Associazione Italiana per la Ricerca sul Cancro, IG31139 to A.M.

COMPETING INTERESTS

JDR and ALV are co-inventors of the patent P2474IT for which they retain no rights of commercial exploitation.

ETHICAL APPROVAL

All experimental methods used in this study were performed in full compliance with the relevant specifications, guidelines, and administrative regulations, as described in the respective sections.

ADDITIONAL INFORMATION

Supplementary information The online version contains supplementary material available at https://doi.org/10.1038/s41418-026-01812-8.

Correspondence and requests for materials should be addressed to JD Rosati or AL Vescovi.

Reprints and permission information is available at http://www.nature.com/reprints

Publisher's note Springer Nature remains neutral with regard to jurisdictional claims in published maps and institutional affiliations.

Open Access This article is licensed under a Creative Commons Attribution 4.0 International License, which permits use, sharing, adaptation, distribution and reproduction in any medium or format, as long as you give appropriate credit to the original author(s) and the source, provide a link to the Creative Commons licence, and indicate if changes were made. The images or other third party material in this article are included in the article's Creative Commons licence, unless indicated otherwise in a credit line to the material. If material is not included in the article's Creative Commons licence and your intended use is not permitted by statutory regulation or exceeds the permitted use, you will need to obtain permission directly from the copyright holder. To view a copy of this licence, visit http://creativecommons.org/licenses/by/4.0/.

© The Author(s) 2026